Materials and Structures (2026) 59:85
https://doi.org/10.1617/s11527-026-02973-1

ORIGINAL ARTICLE

# Acoustic emission testing of prestressed RC bridge girders: methodology, results, and dataset

**Danilo D'Angela · Gennaro Magliulo**

Received: 24 July 2025 / Revised: 7 November 2025 / Accepted: 19 January 2026


**Abstract** The detection of incipient and minor cracks in prestressed reinforced concrete (RC) structures is crucial in ensuring safety of existing bridges. However, traditional structural health monitoring (SHM) often fails to provide reliable and effective early detection. As a matter of fact, literature SHM applications typically investigated moderate-to-severe cracking conditions and often developed criteria that are likely to depend on investigated scenarios. Aiming at addressing the abovementioned literature gap, this study evaluates the effectiveness of acoustic emission (AE) testing for early crack identification in post-tensioned RC girders. AE tests are carried out during cyclic and monotonic four-point bending tests on different specimens up to failure. Multiple AE analysis methods are systematically implemented considering literature methods and novel method specifications (MSs). The evolution of key AE features is examined, and several indicators are further analyzed through a blind assessment framework. The complete AE dataset of AE data is made publicly available. AE activity trends and their potential correlation with observed mechanical damage are identified and discussed. Among the investigated indicators, relative acoustic entropy shows particular promise for early crack detection. The study systematically compares the application of multiple assessment methods, identifying strengths and weaknesses and outlining potential SHM criteria. The findings demonstrate that AE testing, when combined with suitable MSs and damage criteria, offers a viable path for reliable SHM. This paper lays the groundwork for development of robust damage detection criteria.

**Keywords** Structural health monitoring (SHM) · Nondestructive testing (NDT) · Acoustic emissions (AEs) · Acoustic entropy · Reinforced concrete (RC) · Post-tensioned girders

D. D'Angela · G. Magliulo (✉)
Department of Structures for Engineering and Architecture (DIST), University of Naples Federico II (UNINA), Via Claudio 21, 80125 Naples, Italy
e-mail: gmagliul@unina.it

D. D'Angela
e-mail: danilo.dangela@unina.it

G. Magliulo
Construction Technologies Institute (ITC), National Research Council (CNR), Viale Lombardia 49, 20098 Milan, Italy

Published online: 06 February 2026

## 1 Introduction

Effective structural health monitoring (SHM) of prestressed reinforced concrete (RC) members of bridge structures is essential for ensuring their long-term safety and preventing critical damage [1–3]. In particular, SHM criteria must be capable of detecting early signs of damage and degradation, typically not visible by inspections, as identifying moderate to severe cracking may be ineffective to prevent severe

damage and collapse [4], and, in the best scenario, antieconomic. This is critical for prestressed structures and even more critical for post-tensioned girders [5, 6].

In the context of cracking initiation and early development assessment [7], the need for time-continuous monitoring [8], real-time damage assessment [9], and potential remote analysis [10] becomes crucial, since these features allow for (a) potentially immediate and time-continuous detection of issues/alarms, reducing the risk of sudden failures, and (b) more efficient and economic analysis. Among the current SHM techniques, acoustic emission (AE) testing probably is the only technique that has the potential to achieve the abovementioned monitoring goals [11–14].

Very few AE testing applications focused on prestressed girders and specifically investigated cracking phenomena. Yuyama et al. [15] carried out laboratory tests and in-situ applications aiming at detecting and locating failures of steel tendons in post-tensioned RC bridges. They correlated the acoustic activity (amplitude values, number of events) to the wire breaks, discriminating these latter events to hammering and noise; moreover, the event localization was found to be satisfactory. Elfergani et al. [16] performed tests on prestressed concrete (representative of prestressed cylinder pipes), characterizing early corrosion-induced cracking and discerning tensile and shear cracks. Anay et al. [17] tested in-situ prestressed concrete girder bridges and found AE indicators associated with crack formation and propagation during the loading process. Some studies combined AE with other techniques, e.g., digital image correlation (DIC) [18] and ultrasonics [19]. Jiang et al. [18] explored the influence of size and slenderness with regard to failure modes in RC structures, coupling AE and DIC. They provide SHM insights for promisingly improving structural safety and serviceability of real infrastructures. Zhang et al. [20] tested prestressed RC girders coupling AE testing and DIC to assess the shear behavior and damage; they found that AE testing is potentially more effective than alternative traditional techniques in detecting early cracks in prestressed RC girders. Ma and Du [21] applied a deep neural network method to correlate AE features and structural performance, focusing on three-point bending tests on prestressed beams but also accounting for applications to real-world bridges. While the laboratory tests often showed relatively applicable criteria, further effort is needed to improve the application to real structures. Tonelli et al. [12] monitored an existing prestressed concrete bridge span decommissioned but fully representative of current Italian existing bridges. They carried out multiple loading tests and correlated AE features to mechanical conditions and responses of the bridge, identifying precracking presence, crack initiation, and previously achieved maximum load (Kaiser effect and Felicity ratio); the study shows that AE testing is promising for an effective monitoring of real prestressed bridges. Elbatanouny et al. [22] tested in laboratory six identical prestressed RC bridge girders under multiple cyclic tests; the specimens were part of a bridge constructed in 60s and decommissioned after 30–40 years of service. Intensity analysis was implemented by correlating severity and historic indices, considering cumulative signal strength as a reference parameter. Intensity analysis charts were found to be promising for detecting deterioration in both predeteriorated and undeteriorated bridges. Jiang et al. [23] recently tested a ultra-high performance concrete (UHPC) deck of a long-span cable-stayed brid time series and crack propagation and found correlations promising for SHM purposes. They highlighted correlations between AE time series and crack propagation steps, with a focus on the time evolution of $\beta_t$ and b-value, which relate number of AE events with time and with magnitude thresholds, respectively.

In spite of the promising recent advances in AE testing discussed below, several issues limit the application of AE testing and impede its full potential in the context of prestressed RC bridge girders. Literature studies that investigated AE testing with regard to prestressed structures often identified AE parameter correlations that are highly dependent on specific structural configurations, loading protocols, damaging mechanisms, monitoring setup, rather than on generalizable and physically interpretable trends. Consequently, the lack of unified, theoretical-based criteria might limit the broader adoption of AE techniques for damage quantification and classification in prestressed members, also given the significant uncertainty associated with real scenarios. Furthermore, no studies compared acoustic data processed by means of different methods also accounting for different formulations. Finally, very few studies provide technical

references for implementing robust testing procedures in the context of incipient and early cracking damage. Therefore, there is urgent need for a comprehensive investigation that implements AE testing considering a variety of methods, possibly providing for novel and revised method specifications and correlations, to lay the groundwork for the definition of reliable damage assessment methods and criteria. The literature review highlights a critical gap in incipient and early cracking detection, especially if the target is the implementation of methods and data interpretations that are the least biased by specific testing conditions and case-depending empirical observations.

This study addresses the abovementioned literature gap by providing technical guidance for robust AE testing and data processing on complex prestressed RC girders under cyclic and monotonic bending. The focus is on detecting low to moderate damage, particularly concrete cracking. Four girders are tested using four-point bending and blind AE assessment; the raw dataset is also made fully available. The work, part of a broader experimental campaign [6, 24] evaluates both basic and advanced AE techniques, with results discussed through blind assessment and correlated with the mechanical response.

## 2 Experimental tests

### 2.1 Specimens and mechanical tests

The four specimens consisted in girders having same geometry/reinforcement and varying prestressing level, simply defined as S1, S2, S3, and S4. The benchmark specimen details are depicted in Fig. 1. Average concrete compressive strength ($f_{cm}$) was equal to 34.7 MPa, and it was obtained by uniaxial tests on six cubic specimens for each concrete cast. Average concrete Young's modulus ($E_{cm}$) was equal to 32.0 GPa, and it was estimated according to the Eurocode 2 [25]. Ordinary reinforcement properties were derived from the rebar class (B450C) [26], and minimum characteristic (or nominal) yielding strength ($f_{yk}$), minimum characteristic (or nominal) ultimate strength ($f_{tk}$), and average Young's modulus ($E_{sm}$) were equal to 450 MPa, 540 MPa, and 210.000 GPa, respectively. The tendon properties were experimentally estimated according to the relevant regulations as specified by the manufacturers [27]; in particular, stress corresponding to 1% of total deformation ($f_{p,1}$), ultimate strength ($f_{pu}$), and Young's modulus ($E_p$) were equal to 1780 MPa, 1970 MPa, and 203 GPa, respectively.

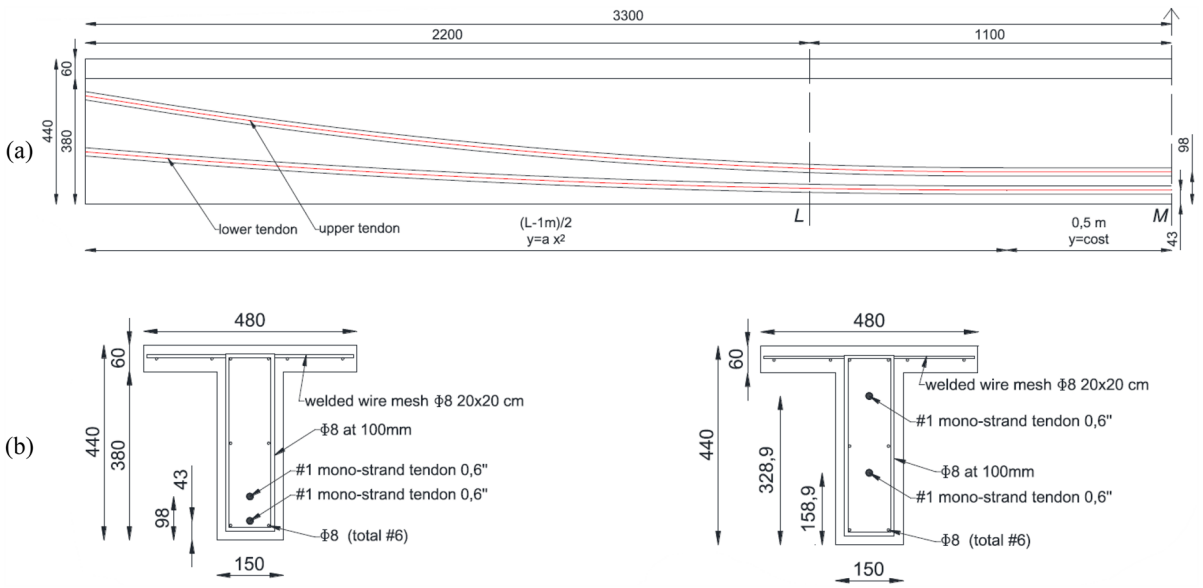


**Fig. 1** Un-strengthened (benchmark) specimen: **a** longitudinal view and **b** midspan (left) and end (right) cross section of the girder (dimension in mm) [6, 24]

S1, S2, S3, and S4 were prestressed by implementing 150, 300, 300, and 150 kN internal prestress force, respectively, according to the procedure already implemented for similar specimens by Losanno et al. [6]. S3 and S4 also presented external post-tensioning, by implementing an external prestress force equal to 100 and 250 kN, respectively, for a total prestress force equal to 400 kN for both S3 and S4 specimens.

Each specimen was tested under four loading conditions, including cyclic (protocol P1) and monotonic (protocol P2) tests. The tests were carried out at the Department of Structures for Engineering and Architecture at the University of Naples Federico II (Italy), and the testing setup is depicted in Fig. 2. The mechanical testing facilities consisted of a rigid steel base, four columns fixed to the foundation floor, and a moving crossbar able to vertically slide, actuated by a servo-hydraulic jack.

P1L1, P1L2, and P1L3 loading conditions consisted in quasi-static force-controlled stepwise two-cycle phases based on P1-protocol [28], corresponding to a maximum applied force ($\max(F_e)$) associated with serviceability, ultimate, and amplified ultimate state conditions [24]. P2 consisted in a quasi-static displacement-controlled monotonic loading condition, implemented up to the earliest achievement between structural failure or maximum stroke of the actuator (150 mm). P1L1, P1L2, P1L3, and P2 are defined as loading protocols in the following.

The applied force ($F_e$) was measured using a load cell, and the midspan vertical displacement of the specimen was measured using a linear variable differential transducer (LVDT) for P1 protocols and with a potentiometer for P2 one.

## 2.2 Acoustic emission tests

### *2.2.1 Apparatus*

The acquisition of the AEs was implemented using the multi-channel AMSY-6 system (VisualAE) produced by Vallen Systeme GmbH. Piezoelectric AE transducers were used, these were able to act as both actuators and sensors, but in the following they will be referred to as sensors. Both non-integrated preamplifier (NIP) and integrated preamplifier (IP) sensors were used, considering low-frequency (VS30) and standard frequency sensors (VS150). VS30 sensor operates within 25 to 80 kHz, having a relatively flat response over this range and resonant at 30 kHz; VS150 sensor works within 100 to 450 Hz and is resonant at 150 kHz. General purpose preamplifiers were used for supporting NIP sensors, setting the gain in order to be consistent with the one implemented for IP sensors.

### *2.2.2 Detection and acquisition*

The sensors were coupled/fastened to the girder surfaces through hot-melt adhesive; the sensor arrangement was verified by performing check and preparation tests, which are described in the following

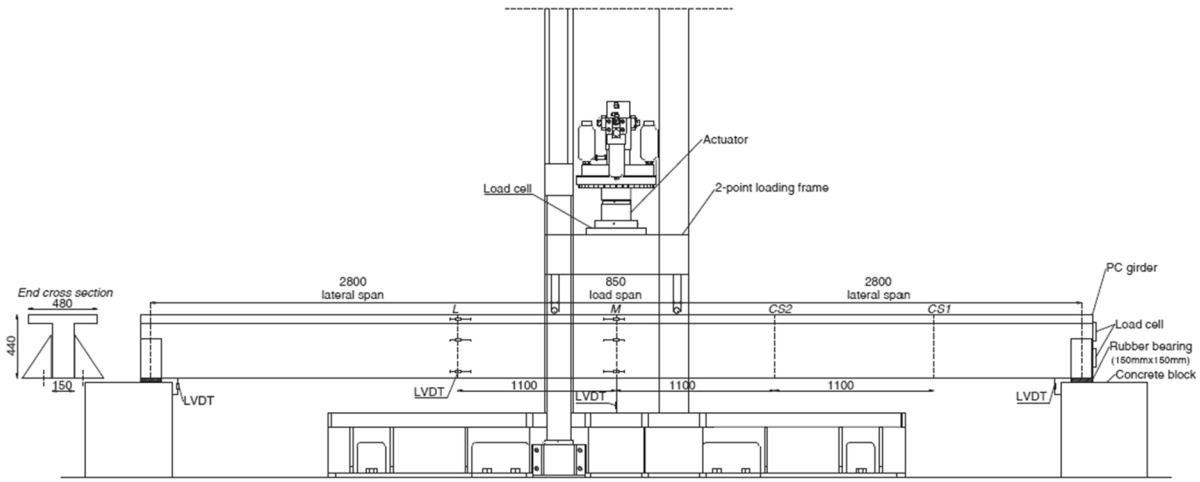


**Fig. 2** Four-point bending testing setup (dimension in mm) [6, 24]

section. The acquisition was implemented through a sampling rate of 10 MHz. The amplitude threshold ($A_{th}$) was set equal to 40 dB and this threshold was set to minimize background and machinery noise during the full functioning of the laboratory facilities; this latter condition was checked during check and preparation tests. An interval of 100 µs was used for defining the number of samples recorded before the first threshold crossing (pre-trigger interval) and after the last threshold crossing (post-trigger interval). Hit definition time (HDT) and hit lockout time (HLT) were set equal to 250 and 2000 µs, respectively, whereas peak detection window was disabled (peak definition time (PDT) was not implemented); maximum hit duration time (MDT) was set equal to 100 ms. A setting band-pass filter was applied to the detected signals, i.e., 25–82 Hz and 75–350 Hz for VS30 and VS150 sensors, respectively. Gain and input setting range were set equal to 34 dB and 10 Vpp, respectively. The abovementioned acquisition parameters were defined by adjusting default settings according to the results of check and preparation tests, considering literature applications as a reference [29–31].

### 2.2.3 *Testing procedure and sensor arrangement*

Check and preparation AE tests were performed on the specimens under rest conditions [32]. These tests consisted of pencil-lead break (PLB) tests, pulsing tests, and localization checks. PLB tests were implemented considering the sensor as a receiver and PLB source as an actuator, applied at multiple distances from the sensor. For each sensor and PLB test it was verified the consistency between the input to output distance and the detected signals, with particular attention to amplitude and energy features. For each sensor, the attenuation law was estimated, and it was assessed to confirm the correct installation. Pulsing tests were carried out to verify the global installation, assessing the consistency between sensors' relative location and pulsing detections; a pulsing test includes a series of $s$ actuation-detection tests, where $s$ is the number of sensors, and each test consists in the generation by each sensor, one at the time, of a standard signal (actuation) while the other sensors detect the propagated signals (detection). Once check and pulsing tests were completed, the localization of the sensors and the attenuation law were implemented in the software. Afterwards, localization tests were performed: multiple PBL tests were carried out generating the input signal within the monitored area and checking that the source localization area was appropriately identified by the localization processing. Whereas 2D localization was approximatively correct in more than 70% of cases, 1D localization was correct in almost all cases. Accordingly, AE setup and instrumentation setting was confirmed to be correctly installed and functioning.

Main AE tests were performed with four channels/sensors, and the type and arrangement of sensors were varied over the different tests, adjusting them according to specific test objectives and ongoing experimentation. For all tests, three sensors were generally located within the midspan area, covering both top and bottom areas of the girder; a sensor was located aside from the midspan, beyond the (left) loading knife section.

Figure 3 shows the type and location arrangement of the sensors for the performed tests. For all specimens, each AE test corresponds to a loading protocol (P1L1, P1L2, P1L3, P2) and to post-tensioning phases (only for S3 and S4). Main AE tests are identified by specimen (S1, S2, S3, S4) and loading protocol (P0, P1L1, P1L2, P1L3, P2), e.g., S1-P1L1, and main AE test data series are identified by specimen (S1, S2, S3, S4), loading protocol (P0, P1L1, P1L2, P1L3, P2), and channel (Ch1, Ch2, Ch3, and Ch4), e.g., S1-P1L1-Ch1.

### 2.2.4 *Basic AE features and filtering*

The following AE features [33] were recorded and elaborated: number of AE events/hits or hits ($H$), peak amplitude or amplitude ($A$), number of counts ($N$), rise time ($RT$), duration ($D$), energy ($E$), root mean square ($RMS$), signal strength ($SS$); cumulative hits ($\Sigma H$), cumulative counts ($\Sigma N$), and cumulative energy ($\Sigma E$) were also considered. $N > N_{min}$ was implemented as a filtering condition for data elaboration, setting $N_{min}$ equal to 3. As a matter of fact, during the pre-tests it was found that significant acoustic activity associated with machine/facility operation and laboratory background presented $N$ not greater than $N_{min}$.

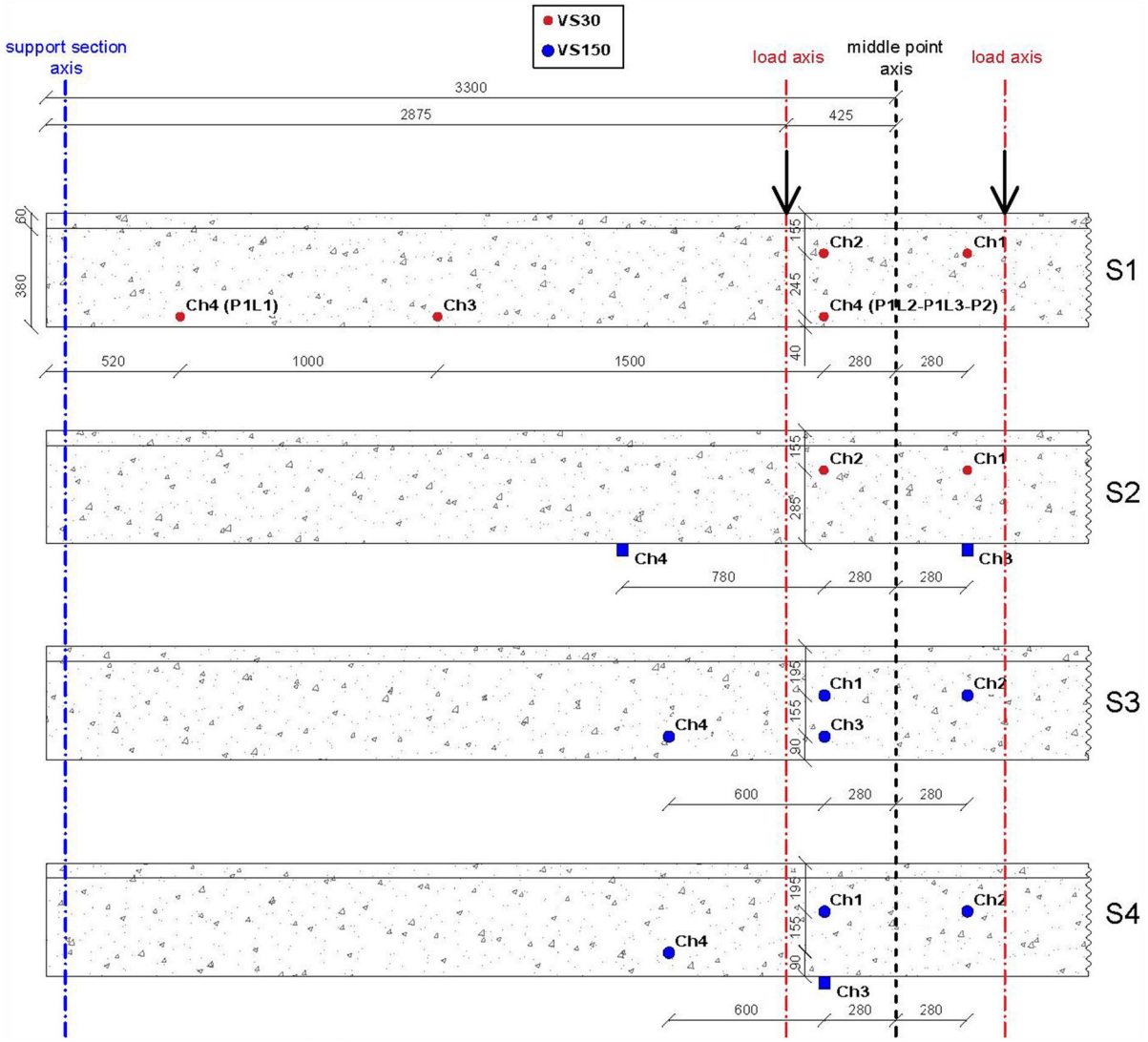


**Fig. 3** Type and location arrangement of sensors associated with tests on all specimens (dimension in mm)

## 3 Acoustic emission analysis

### 3.1 Methodology

AE analysis was implemented through multiple assessment methods and specifications. The implemented assessment methods include the analysis of basic AE activity, Kaiser effect and Felicity ratio, average frequency (*N* to *D* ratio) vs. RA (*RT* to *A* ratio), b-value ($b_{AE}$), and acoustic entropy. The abovementioned methods are described in this section with reference to the literature evidence. Table 1 summarizes all implemented methods and method specifications (MSs); the technical definition of methods, formulations, and notation is discussed in the relevant sections.

#### *3.1.1 Kaiser effect and Felicity ratio*

The Kaiser effect [34] violation potentially informs regarding the damage/degradation condition, quantitatively referring to the Felicity ratio (*FR*), i.e., ratio between the stress/load level associated with (significant) AE activity and the previously reached

**Table 1** Summary of the implemented methods and method specification (MS)

| Method | Specification | | | | Method specification (MS) ID |
|---|---|---|---|---|---|
| | Parameter | | Condition | | |
| Kaiser effect and Felicity ratio | Significant activity descriptor | $\Delta H/\Delta t \geq 3$/s | | | K1 |
| | | AE feature | $N \geq 100$ | | K2.1 |
| | | | $H \geq 10$ & $A \geq 60$ dB | | K2.2 |
| | | $HI \geq 1.4$ | HI: Eq. (2) | no N and K reset | K3.1a |
| | | | | N and K reset at 2nd cycle | K3.1b |
| | | | HI: Eqs. (3) and (4) | no N and K reset | K3.2a |
| | | | | N and K reset at 2nd cycle | K3.2b |
| | | | HI: Eqs. (3) and (5) | no N and K reset | K3.3.a |
| | | | | N and K reset at 2nd cycle | K3.3.b |
| | | | HI: Eqs. (3) and (6) | no N and K reset | K3.4.a |
| | | | | N and K reset at 2nd cycle | K3.4.b |
| RA vs. average frequency | | | | | AFRA |
| b-value ($b_{AE}$) | Subset dataset definition | Current subset dataset | | | b1 |
| | | Cumulative subset dataset | | | b2 |
| Acoustic entropy | Entropy formulation | Shannon | Absolute value ($H_S$) | | E1.1 |
| | | | Cumulative value ($\Sigma H_S$) | | E1.2 |
| | | Kullback–Leibler | Absolute value ($H_{KL}$) | | E2.1 |
| | | | Cumulative value ($\Sigma H_{KL}$) | | E2.2 |

All details regarding methods, formulations, and notation are reported in the relevant sections

maximum stress/load level [35]. During a cyclic loading process, when the structural integrity of the material is affected, *FR* is lower than 1 (Kaiser effect is violated), and *FR* tends to decrease as the damage/degradation process evolves [36], and damage initiation [37] and pre-failure conditions [38] can be associated with threshold values, mostly depending on material and test setup.

The quantitative definition of the onset of significant AE activity is critical in the context of the assessment of the Felicity ratio, especially if the testing environment is relatively noisy and/or the target of the SHM process aims to be relatively accurate. Several specifications were implemented in the literature, based on hits (*H*) vs. time (*T*) evolution [39] or hits rate ($\Delta H/\Delta T$) [40], single- or multiple-event and single/multiple AE feature-based criteria (e.g., considering *N* [41]) or more advanced parameters, e.g., history index (*HI*) [42]. *HI* was developed to quantify the intensity of AEs [43] and it can be referred to as a reliable feature for identifying significant AE activity, in the context of Kaiser effect assessment.

Kaiser effect (violated/non-violated) and Felicity ratio were assessed for each channel, considering each subcycle of the cyclic tests (but the first subcycle of P1L1) and the monotonic procedure. Multiple method specifications (MSs) were implemented to assess the Kaiser effect and to estimate the Felicity ratio (method K), varying the significant activity descriptor: i.e., considering (MS K1) hits rate ($\Delta H/\Delta T$), (MSs K2) single- and multiple-event AE feature-based criteria, and (MSs K3) history index (HI). Table 1 shows the related methodological features. For methods K1, a specification was implemented setting $\Delta H/\Delta T \geq 3$/s (MS K1). Two specifications were implemented for method K2, assuming (MS K2.1) single-event $N \geq 100$ and (MS K2.2) multiple-event $H \geq 10$ and $A \geq 60$ dB. *HI* was assessed according to the formulation reported in Eq. (1), considering an *HI* threshold equal to 1.4, according to consolidated literature (e.g., see Behnia

et al. [42], who focused on RC structures) and Standards (e.g., see [44, 45]). In Eq. (1), $HI\left(\overline{T}\right)$ is $HI$ corresponding to time $\overline{T}$, $\overline{H}$ is the (number of) hits within $T=0$ and $T=\overline{T}$, $S_{0i}$ is $SS$ associated with the $i^{th}$ event, and $K$ in an empirical factor that depends on $\overline{H}$.

$$\mathrm{HI}\left(\overline{\mathrm{T}}\right) = \frac{\overline{\mathrm{H}} \sum_{\mathrm{i=K+1}}^{\overline{\mathrm{H}}} \mathrm{S_{0i}}}{\left(\overline{\mathrm{H}} - \mathrm{K}\right) \sum_{\mathrm{i=1}}^{\overline{\mathrm{H}}} \mathrm{S_{0i}}} \tag{1}$$

Multiple HI-based specifications (MSs K3) were implemented by assuming classical and varied correlations for $K$ since the definition of this latter factor is crucial for the determination of reliable $HI$ values, i.e., (MS K3.1) Eq. (2) reported in the ASTM Standards [46], which is almost identical to the formulation developed by Fowler et al. [43] and is widely used in the literature for RC beams [47], (MS K3.2) Eq. (3) with $\overline{H_1}$ and $\overline{H_2}$ expressed in Eq. (4), defined by Lovejoy [48] who assessed RC bridge girders, and corroborated by Behnia et al. [42] on RC structures, (MS K3.3) Eq. (3) with $\overline{H_1}$ and $\overline{H_2}$ expressed in Eq. (5), and (MS K3.4) Eq. (3) with $\overline{H_1}$ and $\overline{H_2}$ expressed in Eq. (6); these latter two formulation were defined in this study by dividing $\overline{H_1}$ and $\overline{H_2}$ reported in Eq. (4) by 4 and 2, respectively, aiming at implementing Eq. (2) with a lower value of significant events.

$$K = \begin{cases} 0 & \overline{H} \le 50 \\ \overline{H} - 30 & 50 < \overline{H} \le 200 \\ 0.85\overline{H} & 200 < \overline{H} \le 500 \\ \overline{H} - 75 & \overline{H} > 500 \end{cases} \tag{2}$$

$$K = \begin{cases} 0 & \text{if } \overline{H} < \overline{H_1} \\ 0.8\overline{H} & \text{if } \overline{H_1} \le \overline{H} < \overline{H_2} \\ \overline{H} - \overline{H_1} & \text{if } \overline{H} \ge \overline{H_2} \end{cases} \tag{3}$$

$$\left\{\overline{\mathrm{H}_1}, \overline{\mathrm{H}_2}\right\} = \{200, 1000\} \tag{4}$$

$$\left\{\overline{\mathrm{H}_1}, \overline{\mathrm{H}_2}\right\} = \{50, 250\} \tag{5}$$

$$\left\{\overline{\mathrm{H}_1}, \overline{\mathrm{H}_2}\right\} = \{100, 500\} \tag{6}$$

For each MS K3 two different conditions were considered: (a) no AE event ($N$ and $K$) reset within each cyclic test (the two-cycle cyclic tests are considered as a unique detection window) and (b) AE event ($N$ and $K$) reset at the onset of cycle 2 (the two-cycle cyclic tests are considered as composed by two subsequent detection windows (first and second cycle).

### 3.1.2 Average frequency vs. RA

The assessment of $AF$ vs. $RA$ in RC structures potentially allows to characterize the fracture mode since tensile (shear) cracks are typically associated with larger (lower) $RA$ and lower (larger) $AF$ [49, 50]. For concrete beams under flexural loading, the abovementioned fracture mode distinction was often referred to pure tension and mixed (or other crack) mode, to pre-peak stage and macro-crack formation, or to pre-fracture and during fracture rather than tensile and shear cracks [49]. In four-point bending tests of RC beams [51, 52], the opening and development of shear-based cracks is well correlated with the incipience of severe inelastic behavior and major damage. Accordingly, the identification of $AF$ vs. $RA$ clusters associated with the abovementioned crack development is potentially able to detect the abovementioned damage process. In particular, a significant state migration from higher $RA$ and lower $AF$ to lower $RA$ and higher $AF$ can signify the transition between the visible crack formation stage and the distributed crack evolution stage (macrocrack forming preceding the global peak). This behavior is also consistent with cases in which structural behavior is controlled by flexural mechanisms and shear failures are prevented [51].

Another remark that extends the traditional reference to shear cracks in the context of $AF$ vs. $RA$ analysis is associated with the mechanistic correlation between shear and friction in concrete. Recent studies [20, 53] pointed out that AE signatures often associated with shear crack descriptors, including $AF$ and $RA$, should be more consistently referred to a mixture between friction-dominated and tensile mechanisms, implying that it is the friction mechanism that generates AEs more compatible with lower $RA$ and higher $AF$. This specification is more formal than substantial since shear mechanisms in concrete are physically expressed by friction, but it should also be noted that the semantics of “shear crack” implicitly refers to major shear stress fields or shear mechanisms/

failures, whereas the abovementioned cracks and AE signatures are also representative of flexural mechanisms or flexural-controlled failures. It should also be noted that friction occurring is a necessity condition for shear behavior but not necessarily a sufficiency one. In other words, there might be response and damage conditions different from shear mechanisms that are associated with friction; accordingly, AF vs. RA analysis might even be informative regarding the abovementioned conditions. Furthermore, it should be noted that material heterogeneity and wave propagation phenomena could affect the signature of the propagating waves, making tensile-generated cracks looking as shear ones [54], and this is likely to be particularly significant in a non-highly controlled environment (in-situ tests).

In this study, *AF* vs. *RA* response was assessed for identifying the evolution of cracking damage severity levels rather than identifying ongoing fracture modes. Instead of focusing on *AF* vs. *RA* state conditions, the variation of these latter conditions, or better the migration from higher *RA* and lower *AF* to lower *RA* and higher *AF* was meant as a potential assessment method. As a matter of fact, whereas it is quite challenging to define robust generalizable *AF* vs. *RA* correlations to distinguish between tensile and shear cracks, due to geometry, material, sensor location, and response data [51], the abovementioned migration potentially defines a clear and feature-independent transition between low to moderate or moderate to severe, according to the specific rules. In operative terms, for each channel, each loading protocol was divided in subsets, and an *AF* vs. *RA* cluster was identified for each subset, considering the centroid as a cluster reference point. The evolution of this reference point in terms of *AF* and *RA* variations was referred to the subsequent subsets in order to identify potential damage trends, with particular reference to the simultaneous occurring of *AF* decrease and *RA* increase (MS AFRA). Table 1 describes the technical details of the method.

The subsets for P1L1 consist in (1) first cycle first and second increasing (loading) branches, (2) first cycle third and fourth increasing branches, (3) first cycle fifth and sixth increasing branches, (4) (all) first cycle decreasing branches, (5) (all) second cycle increasing branches, and (6) (all) second cycle decreasing branches. For P1L2 and P1L3, subsets include (1) first cycle first increasing (loading) branch, (2) first cycle second and third increasing branches, (3) first cycle fourth and fifth increasing branches, (4) (all) first cycle decreasing branches, (5) (all) second cycle increasing branches, and (6) (all) second cycle decreasing branches. For P2, subsets were defined by considering a number of six equal-time windows up to the achievement of a force equal to 1.5 times the maximum force associated with P1L3.

### *3.1.3 b-value analysis*

Gutenberg-Richter (GR) law [55] correlates earthquake magnitude, $M$, and number of earthquake events having magnitude larger than or equal to $M$, $N_M$, through an exponential empirical correlation, as reported in Eq. (7), where a is an empirical constant and $b$ is the so-called b-value.

$$\mathrm{Log}_{10}\left(\mathrm{N_m}\right) = \mathrm{a} - \mathrm{bM} \tag{7}$$

In the context of AE testing, Eq. (7) can be expressed as reported in Eq. (8) [56, 57], where $H_A$ is the number of AE events (or hits) having (AE) magnitude ($m$) larger than or equal to $m^*$, defining $m$ ($m^*$) as $A$/20 ($A^*$/20), with $A$ ($A^*$) in db, according to the literature (e.g., [58, 59]); $a_{AE}$ is an empirical (AE) constant and $b_{AE}$ is the AE b-value.

$$\mathrm{Log}_{10}\left(\mathrm{H_A}\right) = \mathrm{a_{AE}} - \mathrm{b_{AE}m^*};\mathrm{m^*} = \frac{\mathrm{A^*}}{20} \tag{8}$$

Microcracks are associated with lower amplitudes, leading to higher b-value, whereas when macrocracks form and develop, AEs have higher amplitudes, and this leads to lower b-value [60]. Accordingly, decreases in b-value are potentially expression of transition between microcracking and macrocracking stages. Some Authors were able to quantitatively correlate b-value values and evolution to specific damage stages [61]. For example, b-values in the order of 0.5 or lower can be well correlated to severe damage and incipient failure in RC beams under monotonic flexural loading [56].

b-value was assessed in this study for each channel, over the same subsets considered for the *AF* vs. *RA* analysis. Two MSs were considered to define the datasets associated with each subset, as described in Table 1: (MS b1) considering data from the current subset [58] and (MS b2) accounting for cumulative

data, i.e., current subset and previous ones (cumulative data) [61].

### 3.1.4 Acoustic entropy

The level of microstructural disorder of a mechanical system is measure of damage and degradation state and phenomena, and the analysis of the evolution of this disorder potentially informs regarding the ongoing damage and degradation processes. AEs represents the mechanical/acoustic effect of damage and degradation phenomena and necessarily carry an expression of disorder and chaos [62]. Therefore, assessing AEs by focusing on disorder and chaos metrics potentially allows for identifying robust damage criteria.

In information theory, the (information) entropy measures the amount of uncertainty associated with information within a system or process [63], and in statistical mechanics, information entropy and other disorder/chaos metrics were often correlated to damage and degradation processes within materials, components, and structures [64]. Information entropy associated with AEs is often referred to as acoustic entropy or AE entropy. Recent studies found that the assessment of AE entropy potentially allows to identify and characterize damage and degradation in materials and structures [65, 66], even though only very few preliminary studies applied this technique to RC structural members (e.g., [67]). Even though several methods and formulations were developed in the literature, the classical formulation developed by Shannon [63] is still unsurpassed in terms of simplicity and robustness for AE analysis (e.g., [68, 69]).

Shannon entropy ($H_S$) associated with the $K^{th}$ AE hit is reported in Eq. (9), where $\boldsymbol{p_K}$ is the vector having dimension $K$ that accounts for the probability distribution mass (occurrence probability) associated with the $K^{th}$ AE hit, and $p_K(k)$ is the $k^{th}$ element of vector $\boldsymbol{p_K}$.

$$\mathrm{H_S(K)} = -\sum_{\mathrm{k=1}}^{\mathrm{K}} \mathrm{p_K(k)log_2\left(p_K(k)\right)} \tag{9}$$

$\boldsymbol{p_k}$ is expressed in Eq. (10) $N$ as a feature [62], where $N_i$ represents the (number of) counts related to the $i^{th}$ AE hit.

$$\mathbf{p_K} = \frac{1}{\sum_{\mathrm{i=1}}^{\mathrm{K}} \mathrm{N_i}} \left\{\mathrm{N_1, N_2, \ldots, N_K}\right\} \tag{10}$$

A relative measure of AE entropy that accounts for an historical conditioning between subsequent AE hits can be assessed through the Kullback–Leibler divergence, which was developed by Solomon Kullback and Richard Leibler [70]. Kullback–Leibler entropy ($H_{KL}$) is expressed in Eq. (11) using the same notation of Eq. (9).

$$\begin{aligned}\mathrm{H_{KL}(K)} &= \mathrm{H_S(p_K(k)|p_K(k-1))} \\ &= -\sum_{\mathrm{k=2}}^{\mathrm{K}} \mathrm{p_K(k)log_2}\left(\frac{\mathrm{p_K(k)}}{\mathrm{p_K(k-1)}}\right)\end{aligned} \tag{11}$$

It can be seen that $H_{KL}$ expresses the current ($k^{th}$) event probability mass ($p_k(k)$) as conditioned by the previous ($k\text{-}1th$) event probability mass ($p_k(k\text{-}1)$), differently from $H_S$, which implicitly assumes that each AE hit is an independent event and does not condition the following one [71].

Both $H_S$ and $H_{KL}$ and related cumulative values $\Sigma H_S$ and $\Sigma H_{KL}$ were found to be sensitive to damage and degradation, and potential damage criteria were defined for various materials (often at the material scale) and components (not including RC structures). These criteria were often associated with thresholds, tendencies, and gradients associated with the abovementioned entropy vs. time graphs [8], and, in some cases, these criteria were found to not significantly depend on material, component, and testing condition/arrangement [62, 65]; in particular, it was found that the evolution quality of acoustic entropy is clearly correlated with damage and degradation evolution, and its evolution is not significantly conditioned by the specific application.

Past studies often assessed entropy-based measures considering a dynamic approach (e.g., [72]), i.e., assessing the entropy over shifted detection windows/bin; this computation maximizes the significance of the single detection windows but it might give less weight to historical process and damage accumulation. In this study, the detection windows started from the first AE event and increased including each consequent AE signal as a function of time; accordingly, the entropy measures over time reflected more significantly the historical behavior. This approach was used in past studies considering different materials [62, 69, 73], and it was found to be potentially effective for

damage detection, as well as the related damage criteria were found to be not significantly depending on material/geometry/testing conditions [74].

Acoustic entropy was assessed considering (MS E1.1) $H_S$, the related cumulative value (MS E1.2) $\Sigma H_S$, (MS E2.1) $H_{KL}$, and the related cumulative value (MS E2.2) $\Sigma H_{KL}$ for each specimen/test/channel during testing time; the method details are reported in Table 1.

## 3.2 Results

As discussed in the following sections, at the beginning of P1L1 test of specimen S1, prior to the application of the testing protocol, there was a sudden increase of load due to an unforeseen actuator malfunctioning; this is referred to in the following as pre-test loading. In particular, a sudden applied force with a peak equal to about 28 kN was recorded. For the sake of rigor, this pre-test loading was considered in the study. The present assessment was carried out as a blind prediction, and the only mechanical parameter that was known/considered was $F_e$.

### *3.2.1 Basic activity, Kaiser effect, and Felicity ratio*

Raw acoustic data are made freely accessible at the link provided in the Data availability section. Prior to discussing AEs and comparing different specimen and test results, it should be recalled that (a) sensors' location among the tests was slightly varied over the tested specimens, but all specimens had three sensors within the loading knife sections (two in the top cross-section part and one in the bottom one) and one outside of the middle area (600 to1500 mm far from the left load knife section); (b) V30 (V150) sensors were used for testing S1 (S3 and S4), whereas both V30 and V150 were used for testing S2. Given the similar sensors' location among the different tests and considering that S2 was tested considering both V30 and V150, it is possible to compare the results among the different specimens in a quantitative manner.

AE activity was significantly different among the tested specimens. S1 presented the highest number of events and the highest significance in terms of AE features, e.g., considering *N*, *A*, and *E*. All abovementioned AE features presented maximum values that were often at least an order of magnitude greater than the ones related to other specimens, for all loading protocols. As a representative depiction, *A*, *E*, and $\Sigma H$ are shown along $F_e$ in Fig. 4, Fig. 5, and Fig. 6 respectively. Other AE features were not plotted for the sake of brevity. In subfigures (a) it can be observed the peak force associated with the suddenly applied load at the beginning of P1L1 test of specimen S1, equal to about 28 kN (pre-test loading).

*3.2.1.1 Specimen S1* Overall, *A* and *E* values associated with AEs that occurred corresponding to the pre-test loading related to P1L1 did not exceed 60 dB (Fig. 4) and $10^4$ eu (Fig. 5), respectively, and only an outlier event had *A* slightly larger than 60 dB (Ch2); most events had A lower than 50 dB. $\Sigma H$ at the end of pre-test loading were equal to about 50 and 100, corresponding to sensors Ch1 and Ch2, respectively, and in the order of 10 and 5 for sensors Ch3 and Ch4, respectively (Fig. 4). This response is consistent with the location of the sensors (sensors 1 and 2 were within the loading knife sections, and sensors 3 and 4 were 1500 and 2500 mm from the left loading knife section, respectively; Fig. 1).

During P1L1, no activity was detected up to an applied force equal to about the maximum pre-test force, unless very few outlier events are considered. Accordingly, Kaiser effect was not violated, and this proves that the structural integrity of the specimen was not affected in a sensitive manner by the pre-test loading, even though significant activity was detected. Obviously, maximum *A* (*E*) values were detected at the application of the P1L1 maximum load associated with the first cycle, with maximum *A* (*E*) values equal to about 90 dB ($10^7$ eu) or slightly larger ($10^6$ eu), for Ch1 and Ch2, respectively, and about 80 dB ($10^6$ eu) for Ch3 and Ch4.

Ch1 and Ch2 detect significant activity (with relatively low A and E values) during the first cycle unloading branches, Ch3 and Ch4 only detect very few events. This suggests that the middle section area accumulated damage, more sensibly than other specimen areas, and, since Ch2 detected more significant AE events, it might be possible that the left area of the middle section area is more severely damaged than the right one. Significant AEs were also detected by all channels since the second branch of the second cycle, especially for Ch1 and Ch2, and this highlights a violation of Kaiser effect. This suggests that a load level larger than pre-test maximum force (28 kN) and not larger than maximum load related to P1L1

(35 kN) damaged the specimen in a sensitive manner. Furthermore, it can be observed that several AEs were detected along the decreasing branches related to the second cycle by Ch1 and Ch2, and very few by Ch3 and Ch4, confirming the potential damage accumulation suggested by previously discussed phenomena. Accordingly, it can be reasonably indicated that P1L1 test damaged the specimen and affected its structural integrity. It can also derived that, despite the significant distance between Ch3/Ch4 and middle girder area, considerable AE activity was detected, even though less significant than Ch1 and Ch2 one, and this suggests that (genuine) AEs sourced by crack initiation and evolution propagated for more than 1.5–2 m along the specimen (Ch3 and Ch4 were about 1.8 and 2.8 m far from the middle point of the girder), keeping significant energy.

Similar trends but associated with more significant AE entity are observed over P1L2 and P1L3 tests, and both $A$ and $E$ exhibits critical values, critically larger than the ones detected during P1L1, which increase passing from P1L2 to P1L3. It should be noted that from P1L2 (included) on, sensor 4 was moved at the same vertical of sensor 1, at the bottom cross-section part (Fig. 3). As a matter of fact, AEs associated with Ch4 significantly grow from P1L1 to following tests,

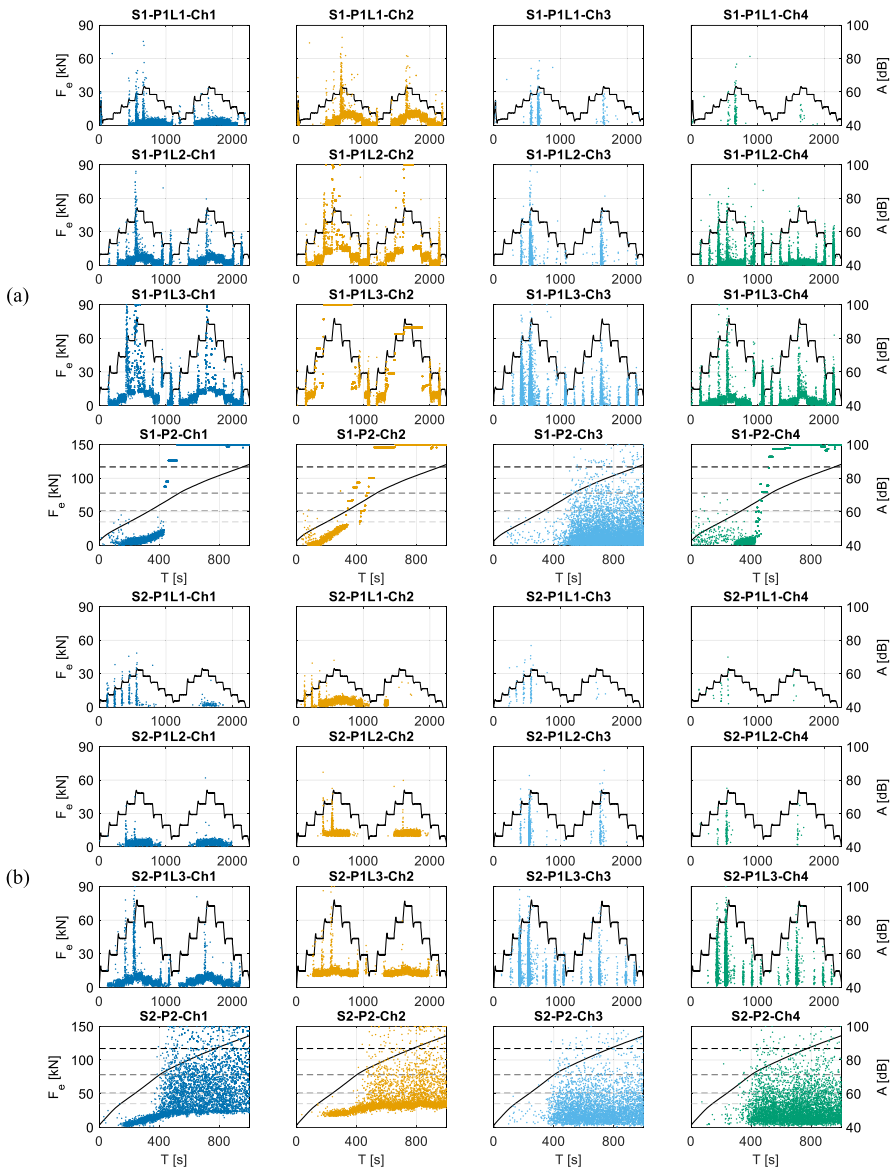


**Fig. 4** Amplitude ($A$) and applied force ($F_e$) vs. time ($T$) for all specimens and loading protocols: **a** S1, **b** S2, **c** S3, and **d** S4

**Fig. 4** (continued)

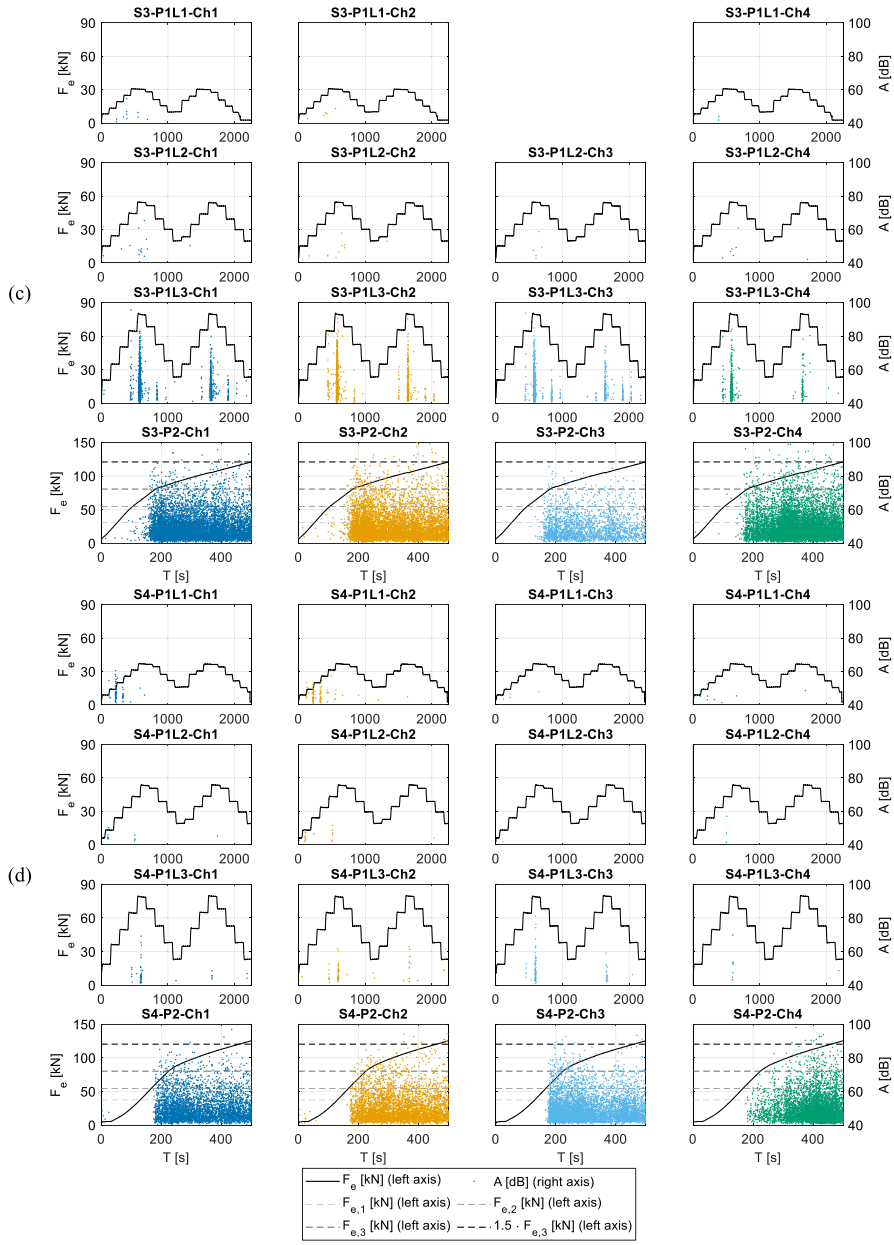


becoming quite similar to other channels, especially in terms of maximum AE feature values. As was also verified during P1L1, Ch2 overall detects higher A and E signals, suggesting that the left side of the middle section area might be more severely damaged, especially over P1L3 test, where Ch3 tends to saturate. The evidence suggests that damage continues to accumulate and becomes more severe passing from P1L1 to P1L2 and from P1L2 to P1L3, and, corresponding to this latter test, it is reasonable to assume that the specimen is severely damaged.

Regarding P2, it can be clearly observed that after an initial time window, all sensors but sensor 3 tend to saturate; time instant and corresponding applied level associated with the onset of the sensors' saturation cannot be univocally determined, but the applied force level is certainly in the order of the maximum force related to P1L3, and this is consistent with the expected behavior. Obviously, prior to this latter force

level, major AE is detected, confirming that major damage affects the specimen since the beginning of P2.

*3.2.1.2 Specimen S2* It should be recalled that for testing S2 sensors V30 were used for Ch1 and Ch2, equal to the ones used for testing S1, whereas sensors VS150 were used for Ch3 and Ch4 (Fig. 3). Therefore, perfectly consistent S1 to S2 comparisons can be made regarding Ch1 and Ch2 (very similar sensors' location and same sensors), and due caution is required to compare Ch3 and Ch4 (different sensors' location and different sensors). AEs associated with specimen S2 showed trends similar to the one related to specimen S1, even though S2 hits and AE feature entity were lower or significantly lower than S1 ones.

The abovementioned lower AE entity is attributable to both different specimen (and mechanical behavior) and different sensors. By comparing Ch1 and Ch2, it can be highlighted the only influence of the specimen, and it can be observed that all significant AE features, e.g., $A$ (Fig. 3), $E$ (Fig. 5), $\Sigma H$ (Fig. 6), and decrease their entity passing from S1 to S2, e.g., maximum $A$ values related to S2 were equal to about 70 dB (Ch1), significantly lower than maximum $A$ values related to S1, larger than 90 dB (Ch2);

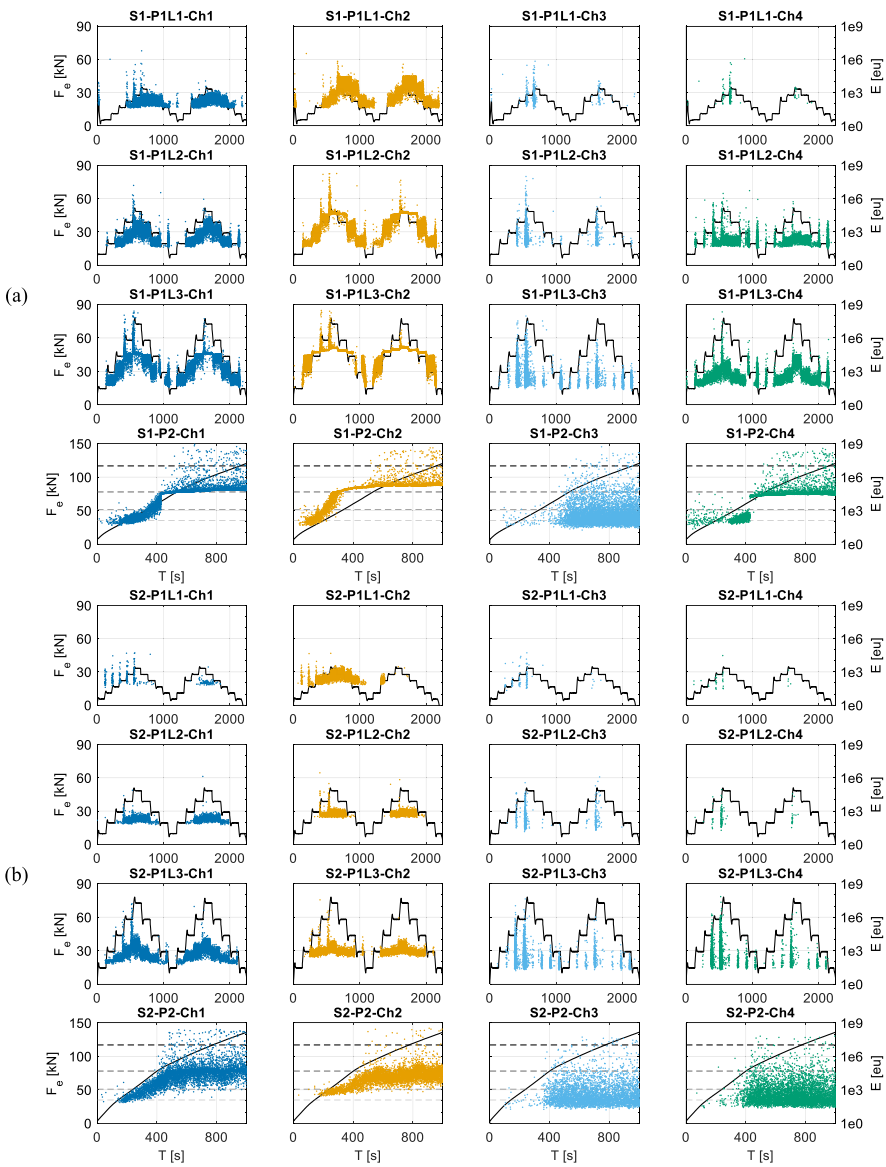


**Fig. 5** Energy ($E$) and applied force ($F_e$) vs. time ($T$) for all specimens and loading protocols: **a** S1, **b** S2, **c** S3, and **d** S4

**Fig. 5** (continued)

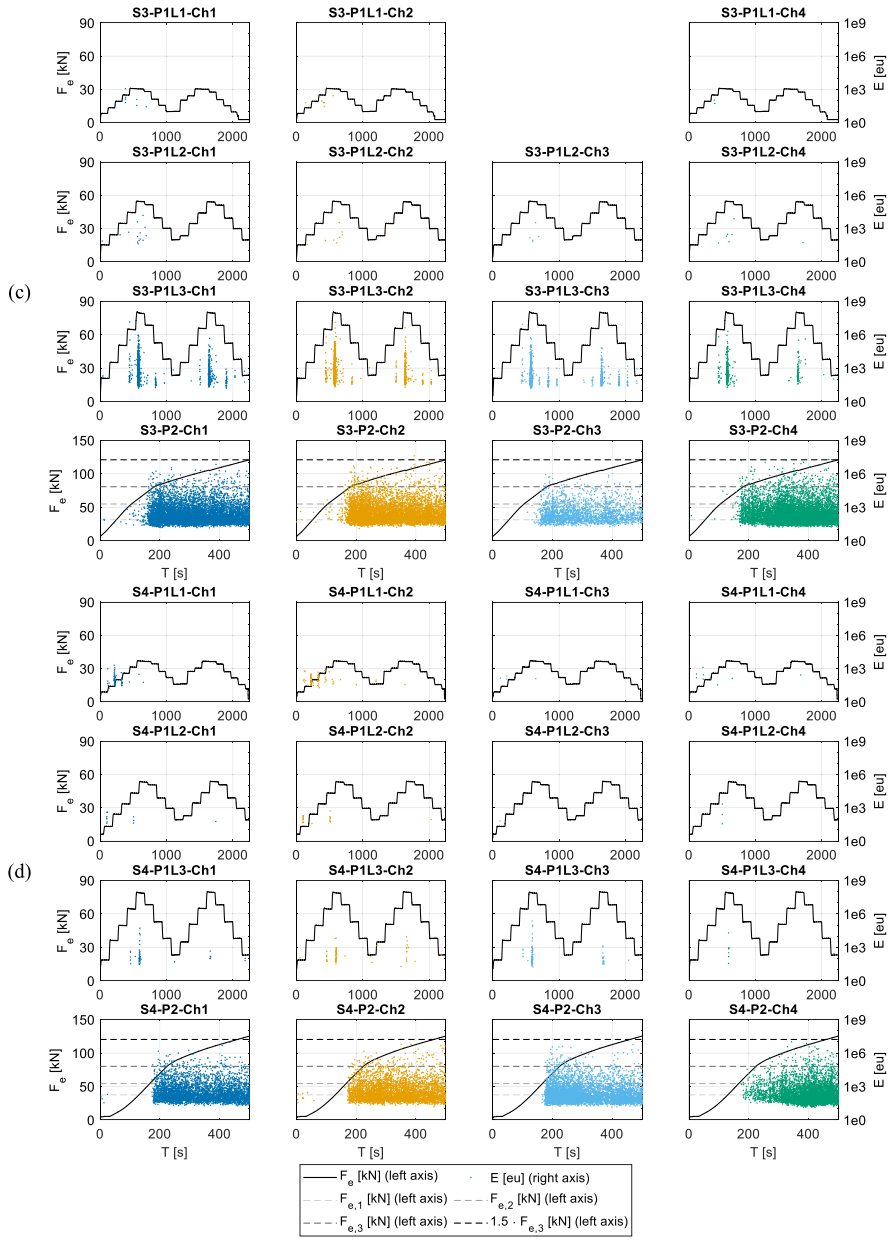


similar trends can be found regarding $E$ values. $\Sigma H$ values related to S2 first cycle peaks are order of magnitude lower than the ones associated with S1. Comparing Ch3 data related to S1 and S2 accounts for both specimen (and mechanical response) and sensor type; it can be observed that even though the same trend associated with Ch1 and Ch2 can be observed by comparing S1 and S2, S2 activity associated with Ch3 is less significant but with lower difference magnitude. This suggests that (a) the specimen (and mechanical response) has less influence outside the middle section area and (b) the sensor's type potentially conditions the entity of AEs but not in a significant manner, and that VS30 and VS150 sensors show similar AE trends. Regarding the influence of the sensor, it can be noted that, overall, VS150 potentially detect less noise or non-genuine AEs, and this can be observed by comparing S1 and S2 AEs (e.g., considering A values showed in Fig. 4) and focusing on lower AE feature values. In particular, Ch3 and

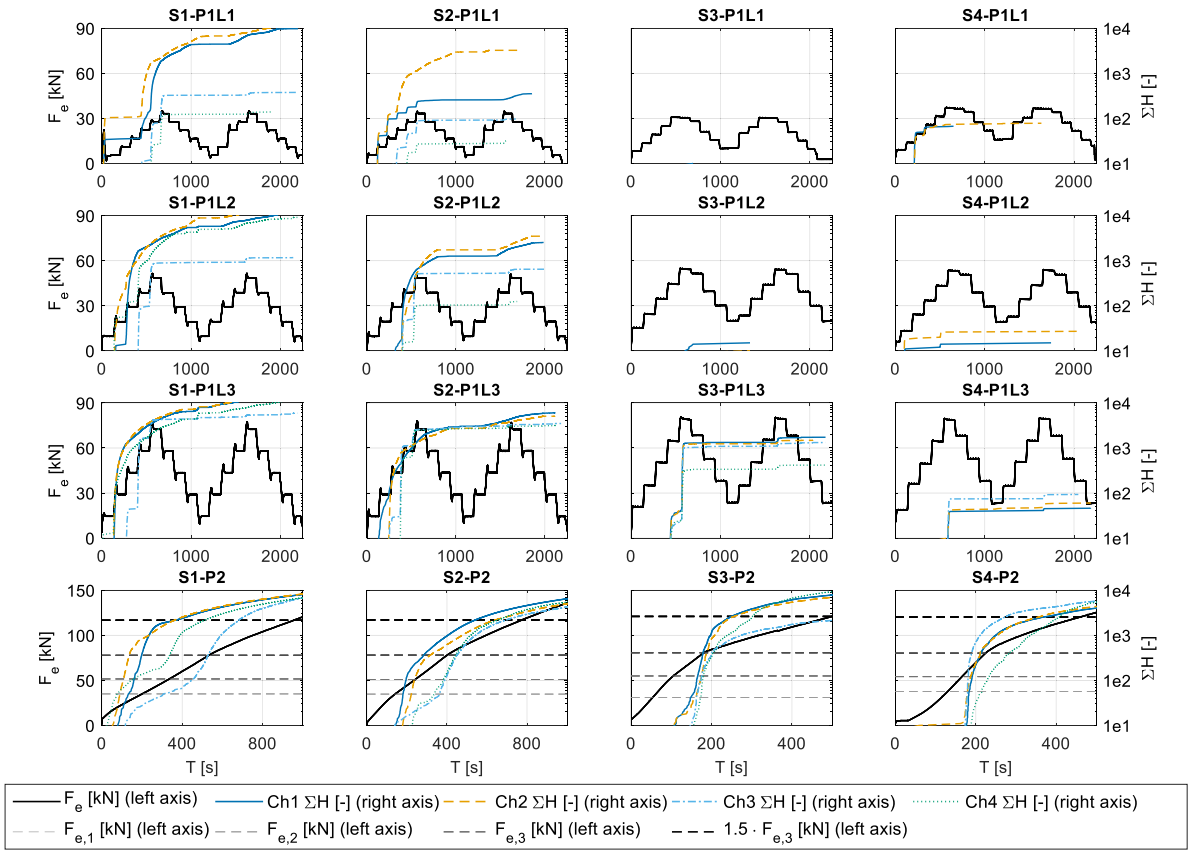


**Fig. 6** Cumulative hits ($\Sigma H$) and applied force ($F_e$) vs. time ($T$) for all specimens and loading protocols

Ch4 (sensor V150) detect high $A$ and high $E$ events, suggesting that a significant part of low $A$ and low $E$ events detected by Ch1 and Ch2 might not be due to genuine damage or degradation conditions.

No loading condition was applied prior to P1L1 for S2, and this is consistent with the observation related to AEs detected from smallest applied load conditions and hits and AEs significance tend to increase during the first cycle increasing loading branches, clearly achieving the maximum values at the maximum applied load. In particular, maximum $A$ values over the different channels range between 65 dB (Ch2) and 78 dB (Ch3), but most AEs corresponding to P1L1 load peak tend to have lower $A$ values. Similarly to S1, S2 AEs show that Kaiser effect is violated since P1L1: some activity, less significant than S1 case, is detected over the second cycle increasing load branch, showing that the specimen might have been damaged over P1L1, even though less significantly than S1 one.

The violation of Kaiser effect associated with S2 P1L1 seems to be less severe than the one related to S1 P1L1 due to the less significant activity observed over the second cycle. This latter activity is more significant looking at Ch1 and Ch2, but it can also be observed considering Ch3 and Ch4. This, once again, confirms that VS30 and VS150 sensors yield similar trends, even though the latter overall detect less activity, and the neglected activity is probably related to noise and non-genuine AEs (i.e., a clear Kaiser effect violation is still clearly detected). Regarding P1L2, it can be observed that no activity is detected up to the third increasing branch related to the first loading cycle, showing that the S2 damage condition associated with P1L1 is probably less significant than S1; as a matter of fact, significant activity was detected since the P1L2 first loading branches related to S1.

The second cycle related to P1L2 also shows a clear Kaiser effect violation, and this clearly indicates that a load level between P1L1 maximum load and P1L2 maximum load significantly conditioned the structural integrity of the specimen. P1L3 results clearly indicate that the structural integrity of the specimen was significantly affected by P1L2: major activity is detected since the first loading branch, as well as it can be observed that P1L3 continues to damage the specimen in a severe manner. Looking at P2 data, it can be observed that damage accumulated by S2 after P1L3 is probably significant (AE is detected since very low load levels) but it might be less severe than the one related to S1 (in this latter case, more significant activity was detected since extremely lower load levels). Even in the case of S2, after an initial time window, the order of magnitude of number of events and AE feature values increases, and the sensors tend to saturate, even though less significantly than S1 case. As it was observed regarding S1, also for S2 the applied force level that corresponds to the onset of the critical AEs is comparable to the maximum load associated with P1L3. This, once again, is compatible with the expected mechanical response of the specimen.

*3.2.1.3 Specimen S3* Very few events were detected during P1L1 test on specimen S3: about 10 events detected by Ch1 and Ch2 and no events and two events detected by Ch3 and Ch4, respectively. These very few events mostly have $A$ ($E$) lower than 50 dB ($10^3$ eu) according to Fig. 4 (Fig. 5), and only an event has $A$ equal to about 55 dB. Few events were detected by all channels during P1L2 test, in the order of 10 for all channels, with amplitudes not exceeding $A$ ($E$) equal to 60 dB ($10^4$ eu), except for a single event, having $A$ ($E$) slightly larger than this latter threshold). A completely different AE trend is observed considering P1L3: (a) significant activity and several events (e.g., in the order of 1000 for each channel) is detected by all channels, with maximum $A$ ($E$) exceeding 85–90 dB ($10^6$ eu); Kaiser effect is moderately to severely violated according to all channels since number of events and AE feature values associated with second cycle are comparable with the ones related to the first cycle. Accordingly, P1L3 clearly affected the structural integrity of the specimen, whereas previous tests did not affect it at all. Negligible activity was detected at the beginning of P2 test, within the initial time window that is upper delimited by an applied force level slightly lower than the maximum applied force related to P1L3. Even though Kaiser effect was clearly violated during the second cycle of P1L3, the fact that for larger force values (P2) it was not violated suggests that the accumulated damage did not critically reduce the structural integrity of the specimen. After the abovementioned upper force level, major activity is detected, with a significant trend that seems to decrease as time increases, especially considering $A$ values; similarly to other specimens, this is probably due to the saturation of the channels due to major overlapping activity.

*3.2.1.4 Specimen S4* AEs detected during tests of S4 are quite similar to the ones related to S3 in terms of trends and AE feature values. Negligible to minor AE activity was detected by all channels during P1L1, and no Kaiser effect violation was observed during the second cycle (only an event was detected by Ch2 and Ch4, but it is meant to be unsignificant). AE features have maximum values comparable to the ones associated with P1L1 test on S3. During P1L2 even less significant activity was observed, if compared to P1L1 one, with less significant AE feature values. Differently from S3, P1L3 associated with S4 shows more activity and more significant AE feature values than P1L2 but still the activity seems to be minor; a very minor Kaiser violation was observed during the second cycle of P1L3, suggesting that the structural integrity of the specimen has been affected but in a negligible to minor entity. Finally, differently from S3, the upper force level associated with significant AE activity onset during P2 is lower than the maximum P1L3 applied force, suggesting that the second cycle related to P1L3 might have continued to affect the structural integrity of the specimen, which accumulated a moderate level of damage.

*3.2.1.5 Kaiser effect and Felicity ratio* A qualitative assessment of Kaiser effect was discussed when the basic AEs were described. In this section, Kaiser effect and Felicity ratio are quantitatively assessed according to the defined MSs (Sect. 0). Multiple MSs were defined but, for the sake of brevity, only MS K3.1b is discussed in this section, whereas all MSs are implemented regarding damage assessment and blind predictions. It is recalled that a Felicity ratio lower than one implies the violation of Kaiser effect,

and the lower is the Felicity ratio (below one) the higher is expected to be the damage condition, as it was discussed in Sect. 0. In particular, the abovementioned conditions were verified for both subcycles of all cyclic tests and for P2 protocol (reported as cycle 1). The quantitative assessment of the Kaiser effect violation, in terms of Felicity ratios, is evidenced in Tables 2, 3, 4 5 for single specimens.

For specimen S1 (Table 2), in all cases but few exceptions mostly associated with Ch3 located at about 1.8 m from the middle point axis of the girder, Kaiser effect is violated, with Felicity ratios that are even lower than 0.5 in several cases. As long as the peak load increases, Felicity ratio clearly tends to decrease, confirming that it is consistently correlated with damage evolution. It is interesting to notice that Ch4, along P1L1, and Ch3, along all tests, are the least sensitive sensors in terms of Felicity ratio trends (decreasing and assuming values lower than unity), and this is fully compatible with their position arrangement (Fig. 3) since they were the farthest ones. In particular, Ch4 under P1L1 (Ch3 under all protocols) was located 2.0 (1.5) m away from the load axis, which defines the boundary condition of the most loaded (in bending) area of the girder. Despite the abovementioned distance, which is certainly a challenge to detect minor cracking initiation and propagation, Ch3 and Ch4 detect values lower than and slightly lower than one along cycle 2 related to P1L1, respectively, as well as they also identify a relevant decrease trend for higher force protocols and always ratio values lower than unity along cycle 2, clearly detecting potential damage, even though with lower severity, as compared to sensors closer to the most damaging area of the girders.

Specimen S2 (Table 3) shows less Kaiser violations and, overall, larger Felicity ratios than S1, especially over protocols P1L1 and P1L2. Given that the peak loads associated with the protocols were the same for all specimens, it can be confirmed that

**Table 2** Kaiser effect violation and Feliciy ratios associated with specimen S1 (MS K3.1b)

| Felicity ratio [–] | S1 | | | | | | | |
|---|---|---|---|---|---|---|---|---|
| | cycle 1 | | | | cycle 2 | | | |
| Protocol | ch 1 | ch 2 | ch 3 | ch 4 | ch 1 | ch 2 | ch 3 | ch 4 |
| P1L1* | **1.24** | 0.24 | **1.25** | **1.50** | 0.63 | 0.59 | 0.86 | 0.99 |
| P1L2 | 0.95 | 0.88 | **1.20** | 0.61 | 0.37 | 0.20 | 0.61 | 0.33 |
| P1L3 | 0.85 | 0.53 | **1.00** | 0.81 | 0.23 | 0.20 | 0.27 | 0.20 |
| P2 | 0.40 | 0.41 | 0.72 | 0.30 | NA | NA | NA | NA |

A Felicity ratio lower than one implies that Kaiser effect is violated. Kaiser effect non-violation is highlighted with bold values

*Prior to P1L1 an accidental pre-test loading condition was applied; therefore, Kaiser effect was also checked with regard to first subcycle of this protocol

**P2 data (cycle 1) are associated with a detection window that extends up to the maximum force level associated with P1L3

**Table 3** Kaiser effect violation and Feliciy ratios associated with specimen S2 (MS K3.1b)

| Felicity ratio [–] | S2 | | | | | | | |
|---|---|---|---|---|---|---|---|---|
| | cycle 1 | | | | cycle 2 | | | |
| Protocol | ch 1 | ch 2 | ch 3 | ch 4 | ch 1 | ch 2 | ch 3 | ch 4 |
| P1L1 | NA | NA | NA | NA | 0.84 | 0.65 | **1.02** | **1.02** |
| P1L2 | 0.95 | **1.23** | **1.23** | **1.34** | 0.63 | 0.60 | 0.60 | 0.81 |
| P1L3 | 0.60 | 0.90 | 0.90 | 0.90 | 0.20 | 0.20 | 0.20 | 0.40 |
| P2* | 0.70 | 0.86 | 0.99 | 0.93 | NA | NA | NA | NA |

A Felicity ratio lower than one implies that Kaiser effect is violated. Kaiser effect non-violation is highlighted with bold values

*P2 data (cycle 1) are associated with a detection window that extends up to the maximum force level associated with P1L3

**Table 4** Kaiser effect violation and Feliciy ratios associated with specimen S3 (MS K3.1b)

| Felicity ratio [–] | S3 | | | | | | | |
|---|---|---|---|---|---|---|---|---|
| | cycle 1 | | | | cycle 2 | | | |
| Protocol | ch 1 | ch 2 | ch 3 | ch 4 | ch 1 | ch 2 | ch 3 | ch 4 |
| P1L1 | NA | NA | NA | NA | NA | NA | NA | NA |
| P1L2 | NA | NA | NA | NA | NA | NA | NA | NA |
| P1L3 | **1.47** | **1.47** | **1.47** | **1.48** | **1.01** | 0.83 | 0.86 | 0.83 |
| P2* | 0.92 | 0.94 | 0.95 | **1.00** | NA | NA | NA | NA |

A Felicity ratio lower than one implies that Kaiser effect is violated. Kaiser effect non-violation is highlighted with bold values

*P2 data (cycle 1) are associated with a detection window that extends up to the maximum force level associated with P1L3

**Table 5** Kaiser effect violation and Feliciy ratios associated with specimen S4 (MS K3.1b)

| Felicity ratio [–] | S4 | | | | | | | |
|---|---|---|---|---|---|---|---|---|
| | cycle 1 | | | | cycle 2 | | | |
| Protocol | ch 1 | ch 2 | ch 3 | ch 4 | ch 1 | ch 2 | ch 3 | ch 4 |
| P1L1 | NA | NA | NA | NA | NA | 1.01 | NA | NA |
| P1L2 | NA | NA | NA | NA | NA | NA | NA | NA |
| P1L3 | NA | **1.50** | **1.49** | NA | **1.00** | 0.82 | **1.01** | NA |
| P2* | 0.78 | 0.81 | 0.78 | 0.98 | NA | NA | NA | NA |

A Felicity ratio lower than one implies that Kaiser effect is violated. Kaiser effect non-violation is highlighted with bold values

*P2 data (cycle 1) are associated with a detection window that extends up to the maximum force level associated with P1L3

specimen S2 was less damaged than S1, even though it certainly exhibited damage since the first protocols.

Very fewer Kaiser effect violations and larger Felicity ratios were observed for specimens S3 (Table 4) and S4 (Table 5), as compared to specimens S1 and S2, and the earliest violations are associated with the second cycle of protocol P1L3; prior to this load conditions, Felicity ratio is significantly larger than one, highlighting that the specimens were not sensible affected by damage up to this latter condition. Violations associated with P2 exhibit relatively large Felicity ratio, suggesting that minor damage might have occurred.

*3.2.1.6 Discussion remarks* The analysis of the basic features suggests that AEs can be well correlated to the mechanical response of the specimen, with particular attention to damage accumulation and structural integrity. In some cases, it seems that AE events and features might reflect the damage accumulation level. The results are discussed in Sect. 4 with regard to the experimental response, confirming whether the potential correlations are effective or not. It should be noted that the abovementioned hypotheses regarding the damage were made downstream of the tests and account for the comparison among the different tests. Furthermore, even though some qualitative potentially damage-correlated AE feature trends and thresholds were defined, as it was expected, these do not potentially allow defining robust damage criteria for structural health monitoring purposes. Similarly, the assessment of Kaiser effect and the estimation of Felicity ratio clearly suggest potential damage accumulation and structural integrity detriment evolutions, especially with regard to comparisons and relative evaluations, and the related potential correlations are qualitatively compatible with the observed AE trends and features. The assessment of Kaiser effect and Felicity ratio is clearly physical-based and was found to be potentially meaningful and coherent with the mechanical response, even though it necessarily requires knowing the loading level of the applied

cycles. This latter condition is applicable in the context of static testing of structures and infrastructures, when the application of the load is controlled, and the tested facility can be monitored over its application [75, 76]. Therefore, basic AE analysis and associated features (Kaiser effect and Felicity ratio) do not seem to be potentially effective for passive monitoring purposes (main objective of AE testing), unless the monitoring target is associated with relative damageability among homologous components or qualitative alarms.

### 3.2.2 *RA vs. average frequency*

*AF* vs. *RA* was assessed along the investigated subsets for all tests on all specimens. The representative results associated with specimen S1 are shown in Fig. 7; the median points of each cloud are also plotted for all subsets in which at least three AE events were recorded. Both lognormally fitted median and empirical median points, represented by *mLN* and *mE* were considered; the former was computed according to the well-known lognormal model provided by Porter et al. [77] and the latter simply represents the empirically observed median value. Median point was considered instead of centroid (mean point) in order to not account for outlier data. As it can be observed in Fig. 7 (associated with specimen S1 and protocol P1L1), data clouds and related median point tend to migrate towards lower *AF* and higher *RA* values along the investigated subsets. In particular, the migration of the cloud median point was expressed as a function of the subsequent subsets by decoupling *AF* and *RA* to quantitatively assess the

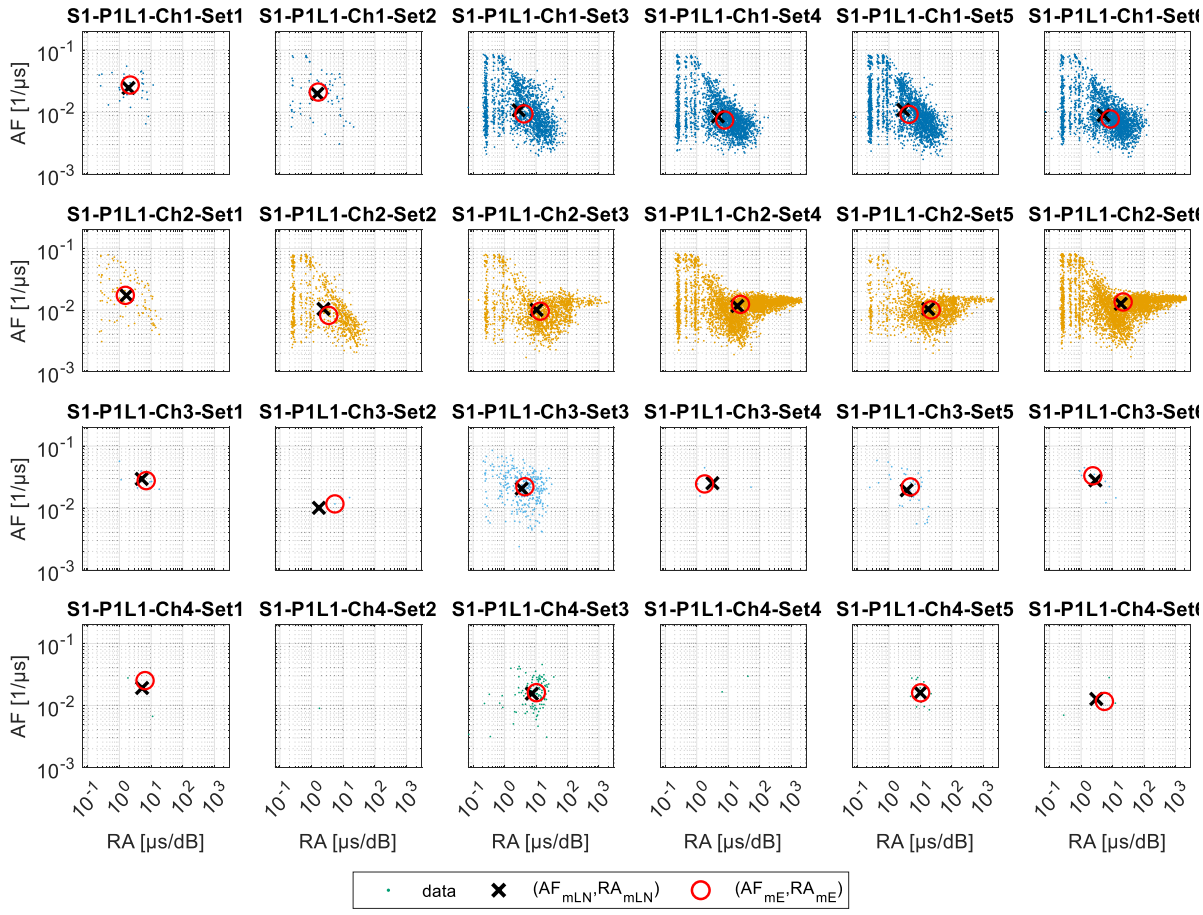


**Fig. 7** Average frequency (*AF*) vs. rise time to amplitude ratio (*RA*) along subsequent subsets and subset median points (*mLN* and *mE*) associated with tests on T1 specimen under P1L1 loading protocol (MS AFRA)

abovementioned data cloud migration, according to the literature evidence (Sect. 1.1.1).

The elaborations related to all specimens are depicted in Fig. 8. The most evident results are associated with a different order of magnitude for *RA* values associated with VS30 and VS150 sensors detections: the former sensors (Ch 1 to Ch4 for S1 and Ch1 and C2 for S2) are associated with *RA* values significantly larger than the ones related to the latter sensors (all other cases). This can be clearly observed by identifying the *RA* value range similarities of Ch1 and Ch2 curves related to Fig. 8a and Fig. 8b, associated with VS30 sensors, and comparing these values with Ch3 and Ch4 curves in Fig. 8b and all channel figures in Fig. 8d, which correspond to VS150 sensors. Despite the differences in terms of values, the *RA* trends related toVS30 and VS150 sensors are overall similar, as it can be observed in Fig. 8b comparing Ch1-Ch2 and Ch3-Ch2 variation signs along consequent subsets. *AF* value ranges and variation trends do not seem to be conditioned by the sensors' sensitivity since *AF* value ranges are comparable among different sensor curves. The abovementioned evidence suggest that different sensor frequency sensitivity does not significantly condition the trend variation of *RA* and *AF* parameters along consequent subsets, and, as a consequence, damage criteria based on variation signs rather than on values might be meaningful over AEs detected through different sensors (with regard to VS30 and VS150 ones). Some subsets exhibit more pronounced shifts in terms of *RA* increasing and *AF* decreasing, which, in some cases, for example S1 specimen results, are concurrent.

Bending of post-tensioned prestressed girders produces a complex stress–strain state that favors the development of mixed-mode stress/strain phenomena and cracks since service loading conditions, differently from ordinary RC beams that typically tend to initiate and develop cracking through a relatively regular migration from tensile to crack mode and single- to mixed-mode fracture response. Conversely, when post-tensioned girders initiate to exhibit macrocracking and it does spread, e.g., beyond service conditions and towards ultimate conditions, a shear and friction signatures might become more significant and a transition in stress–strain phenomena and cracks might be observed, even though with less significance than for ordinary beams. The abovementioned mechanical

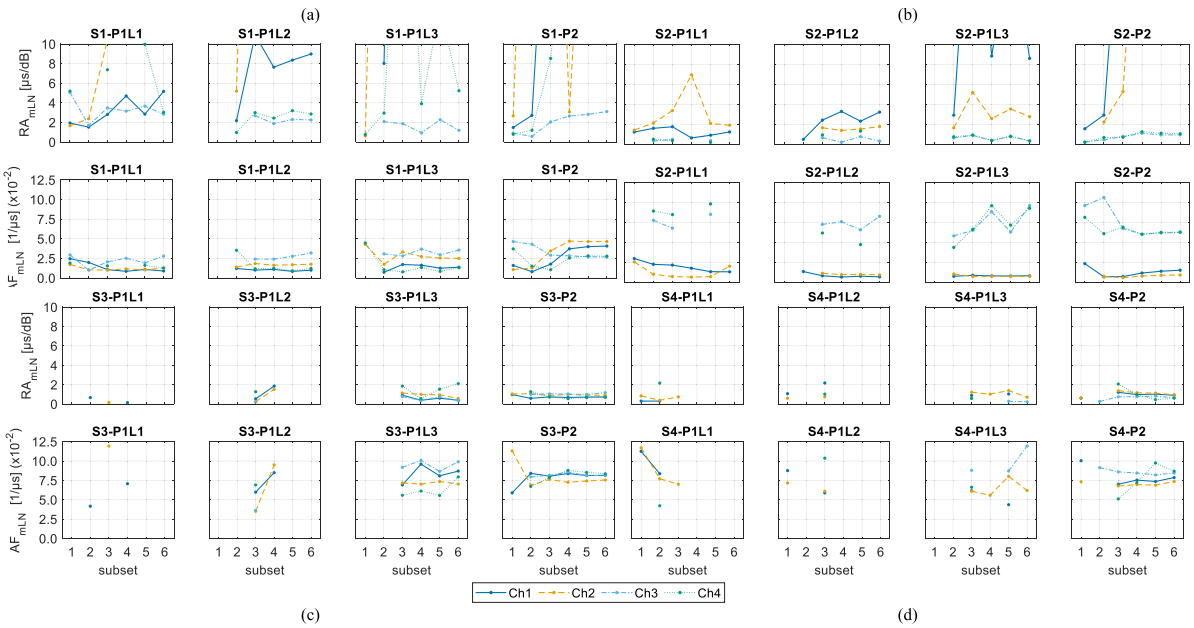


**Fig. 8** Average frequency (*AF*) and rise time to amplitude ratio (*RA*) associated with data cloud median points (*mLN*) vs. subsequent subsets associated with loading protocols and specimens **a** S1, **b** S2, **c** S3, and **d** S4 (MS AFRA). P2 data are associated with a detection window that extends up to the maximum force level associated with P1L3; median point is referred to *mLN*, i.e., lognormal fitting median

specifications are discussed in the following section accounting for the disclosed experimental response of the tested beams.

### 3.2.3 b-value analysis

The correlation between $H_A$ and $A$ (or $m$) was assessed for all tests and specimens, along the investigated subsets, and best-fit loglinear curves were found to estimate $b_{AE}$. Figure 9 shows representative results related to cyclic tests on specimen S1, considering data from current subsets (MS b1). The evolution of $b_{AE}$ along the subsequent subsets is quantified in Fig. 10 considering all specimens. According to the literature, two tendencies highlighted in Fig. 10 can be assessed within each subset to potentially identify damage criteria: (a) achievement of lower values of $b_{AE}$ and (b) $b_{AE}$ decreasing along subsequent subsets. As it was discussed in Sect. 1.1.2, condition (a) can be expressed as considering $b_{AE} \leq 1$.

### 3.2.4 Acoustic entropy

Acoustic entropy was assessed as a function of time for all tests and considering each channel. Figure 11 shows $H_S$ (MS E1.1) and $H_{KL}$ (MS E2.1) as a function of $T$ for the representative case of specimen S3. Over cyclic tests, $H_S$ (Fig. 11a) mostly increases during the first cycle reaching a plateau at the achievement of the peak load, and this is compliant with the fact that this cycle is overall more significant in terms of accumulated damage. The channel location does not significantly affect the $H_S$ since tendencies and maximum values are comparable over different tests. The $H_S$ peak values increase as the cyclic peak load increases, and this is also possibly consistent with the

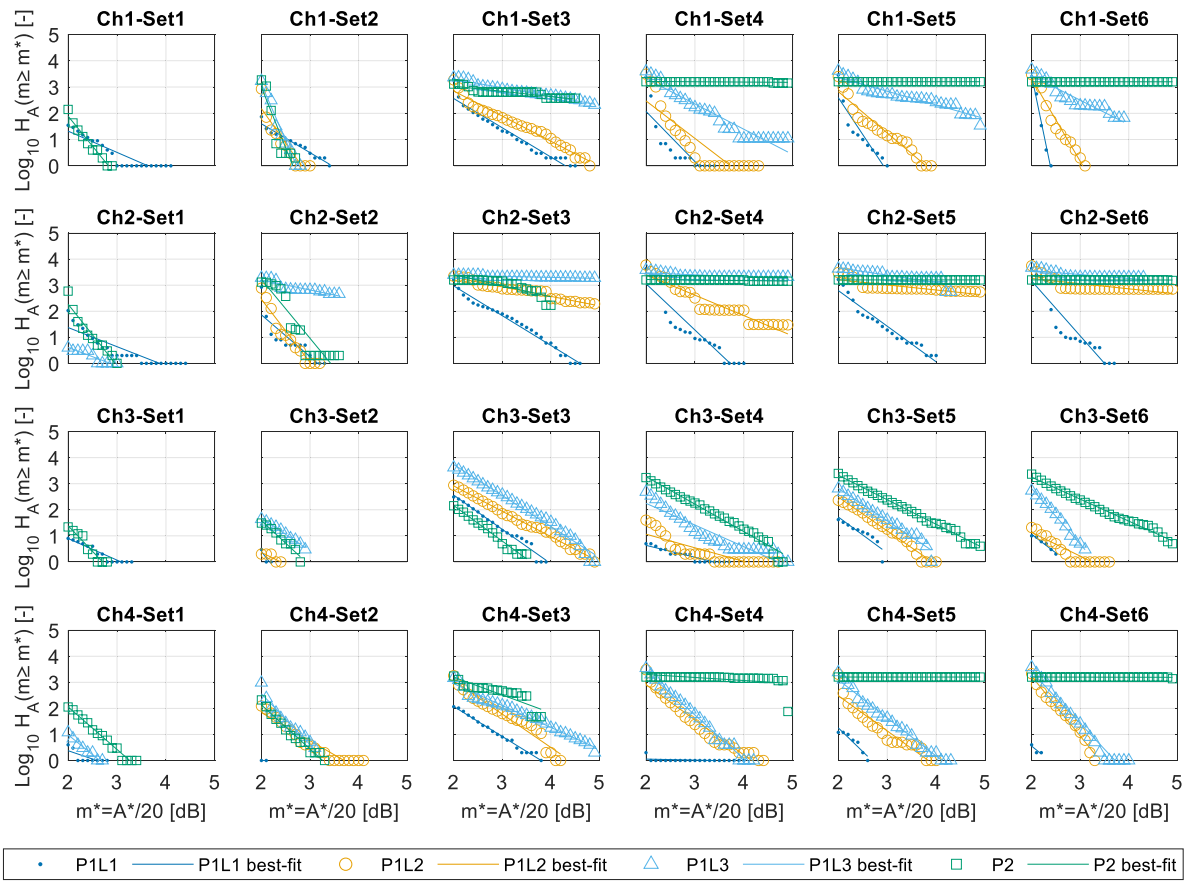


**Fig. 9** b-value analysis: hits having amplitude larger than or equal to A* ($H_A$) vs. $m^* = A^*/20$ and related loglinear best-fit curves associated with cyclic tests along subsequent subsets, considering data from the current subset (MS b1), related to specimen S1

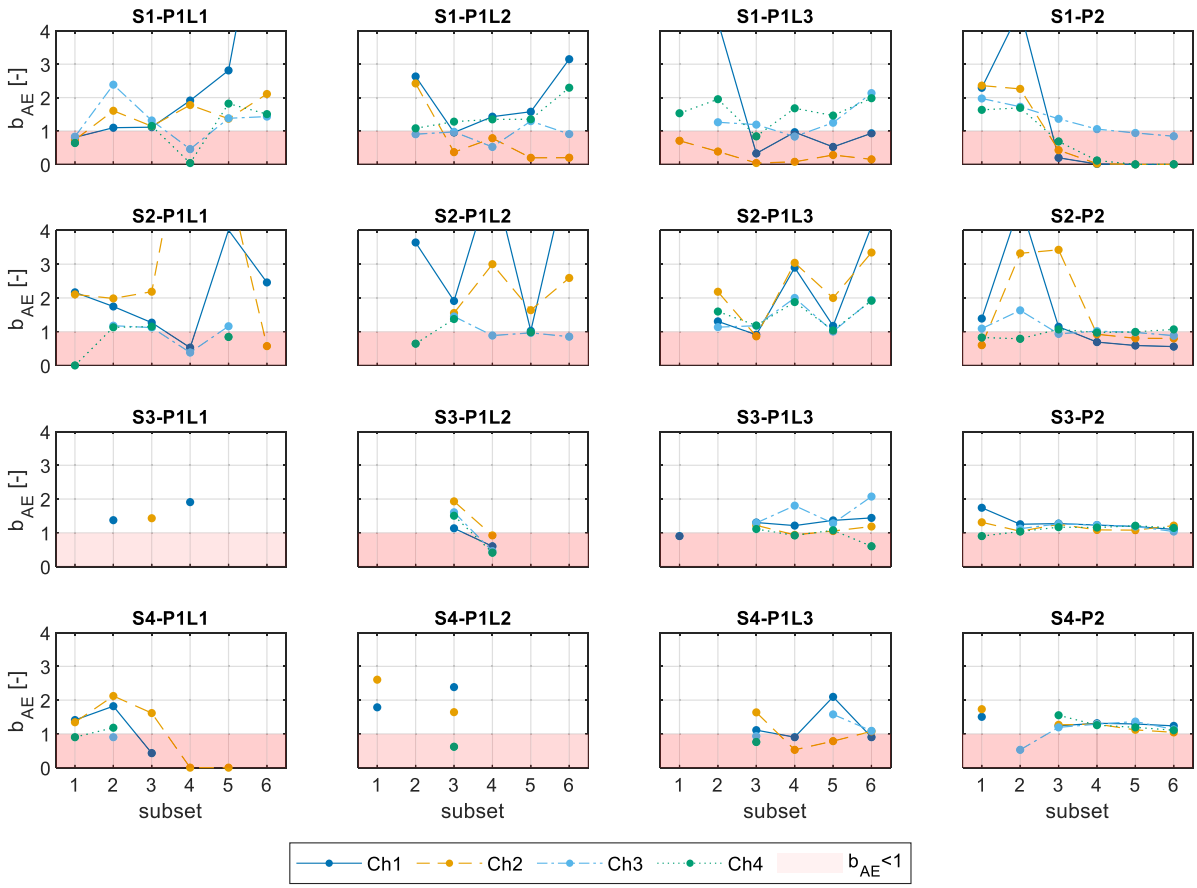


**Fig. 10** b-value ($b_{AE}$) vs. subsequent subsets considering data from the current subset (MS b1), related to specimens **a** S1, **b** S2, **c** S3, and **d** S4

potential damage accumulation trend. Over P2 test, it can be observed that all sensors achieve the same $H_S$ value corresponding to the peak load associated with P1L2, whereas, at P1L3 level, Ch3 is associated with a $H_S$ value that is lower than the other sensors one, and this suggests that the damage accumulates more significantly in sensors other than Ch3, which is located below the specimen. In fact, cracks initiate at the lower bound of the specimen (closely to Ch3) and evolve toward the upper bound (getting closer to Ch1 and Ch2) and also propagate towards the girder supports (getting closer to Ch4). Accordingly, it could be hypothesized that $H_S$ growing is associated with occurring with damaging mechanisms that have an entity correlated to the ongoing $H_S$ value, whereas post-growing plateau responses, corresponding to relatively high $H_S$ values, might be expression of significant accumulated damage with not significant ongoing damage. The abovementioned hypotheses are clearly compatible with previous qualitative remarks.

A completely different trend can be observed considering $H_{KL}$ (Fig. 11b). Since the first cyclic tests, high value $H_{KL}$ peaks are observed, and these peak values are comparable over different sensors, protocols, and specimens. It is interesting to note that after peak values are achieved, $H_{KL}$ tends to decrease, and this is also observed with regard to P2 test, which is certainly associated with damage accumulation over time. The formulation of $H_{KL}$ accounts for a relative measure of entropy, which computes the current event (absolute) entropy conditioning that to the previous event; therefore, as a relative measure, it was expected that its quantitative entity is strongly affected by the

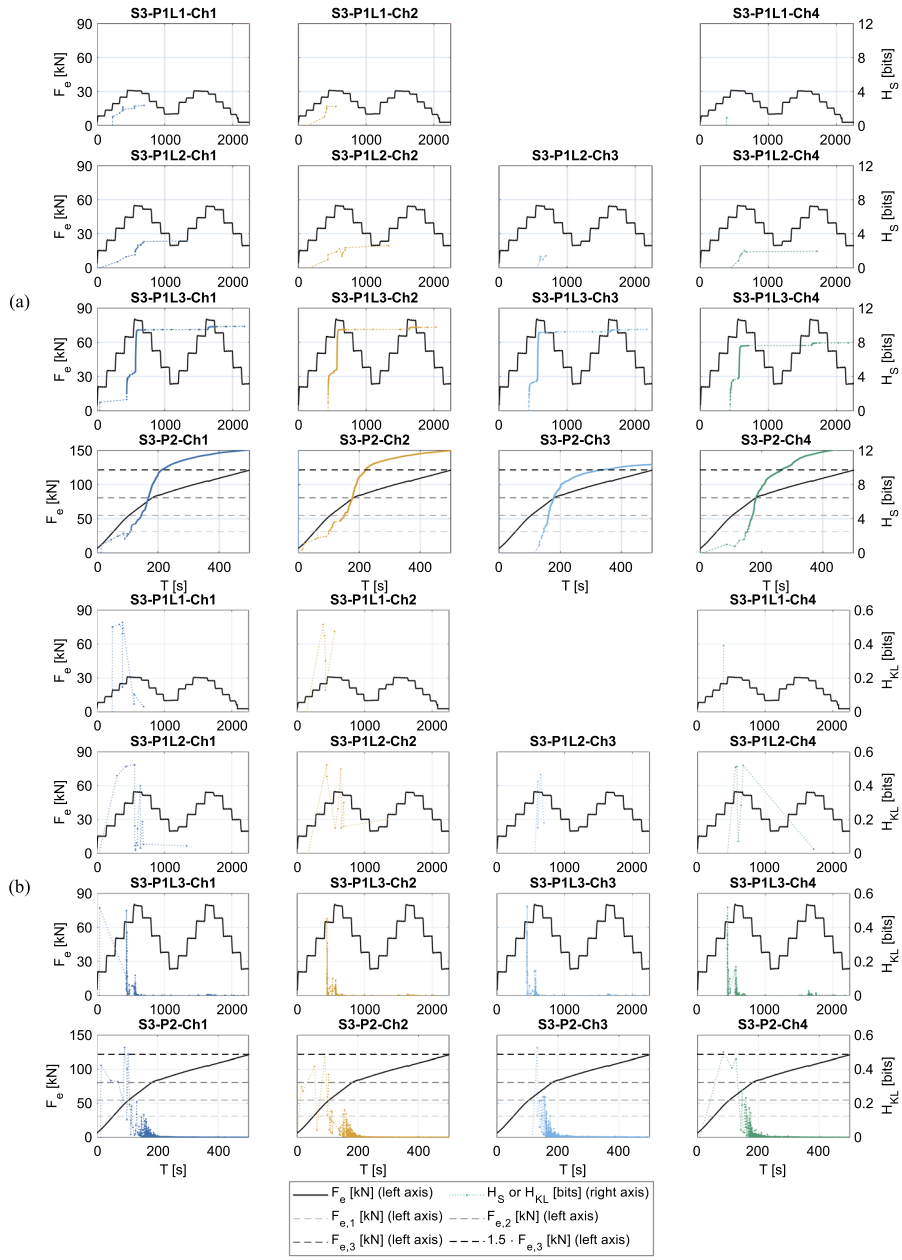


**Fig. 11** **a** Shannon entropy ($H_S$) (MS E1.1) and **b** Kullback–Leibler entropy ($H_{KL}$) (MS E2.1) and applied force ($F_e$) vs. time ($T$) for specimen S3 and loading protocols

ongoing process. In other words, $H_{KL}$ is expected to be more sensitive to the state variation referred to the current state values rather than to the absolute value of the variation. This conceptual interpretation appears to be consistent with the abovementioned observations: higher peak $H_{KL}$ might correspond to damage initiation phenomena rather than to damage evolution ones. Accordingly, a cumulative value of $H_{KL}$ would potentially carry the integral information associated with relative state variation expressed along the ongoing process.

Figures 11 and 12 show $\Sigma H_S$ (MS E1.2) and $\Sigma H_{KL}$ (MS E2.2) as a function of $T$ for all specimens/tests and channels. Among the possible observations, the following remarks can be discussed. In most cases, when cumulative entropy increases, the increase is extremely large and sudden in terms of time. This might suggest that entropy is sensitive to incipient

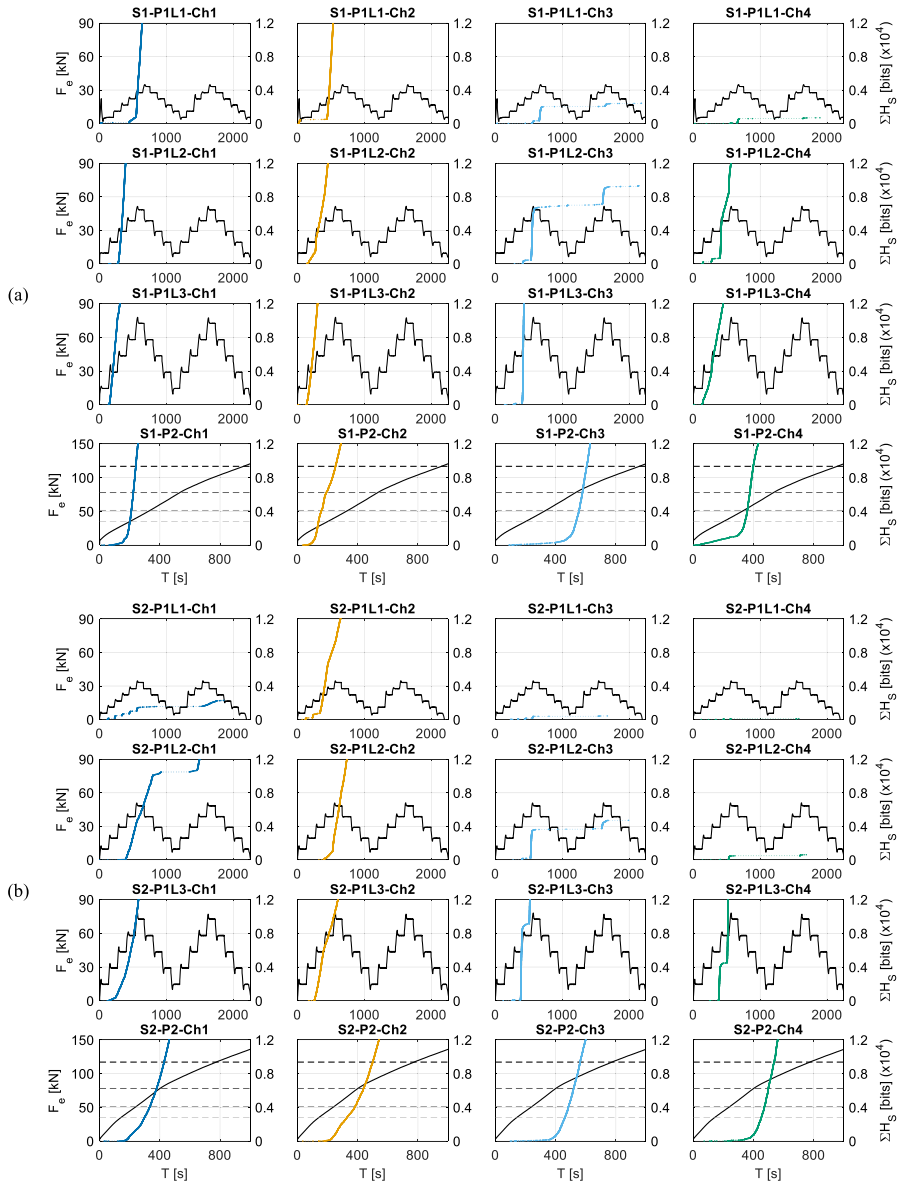


**Fig. 12** Cumulative value of Shannon entropy ($\Sigma H_S$) (MS E1.2) and applied force ($F_e$) vs. time ($T$) for all specimens and loading protocols: **a** S1, **b** S2, **c** S3, and **d** S4

damage and once it is "activated" is clearly shows it. Despite second cycles of loading are associated with AE features comparable with first cycles ones in some cases, e.g., for specimens S1 and S2, entropy parameters associated with second cycles are overall less significant than first cycle ones, and this is consistent with the fact that first cycles are more responsible for damage than second ones since previously reached peak forces are always exceeded during first cycles. $\Sigma H_{KL}$ seems to be less sensitive than $\Sigma H_S$ to the distance between sensor and damaged area. For example, this can be observed considering P1L1 test on S1: both $\Sigma H_S$ and $\Sigma H_{KL}$ clearly reflect that Ch4 is (Ch1 and Ch2 are) the farthest (closest) to the damaged area, with Ch3 at an intermediate distance, but $\Sigma H_S$ yields extremely low (high) maximum entropy values with regard to Ch4 (Ch1 and Ch2), showing a significant sensitivity to the distance, whereas $\Sigma H_{KL}$ values are more comparable among the different distances from the damaged area. In other words, $\Sigma H_{KL}$ seems to valorize more sensibly sourcing mechanisms than distances from the damaged area, and this might

**Fig. 12** (continued)

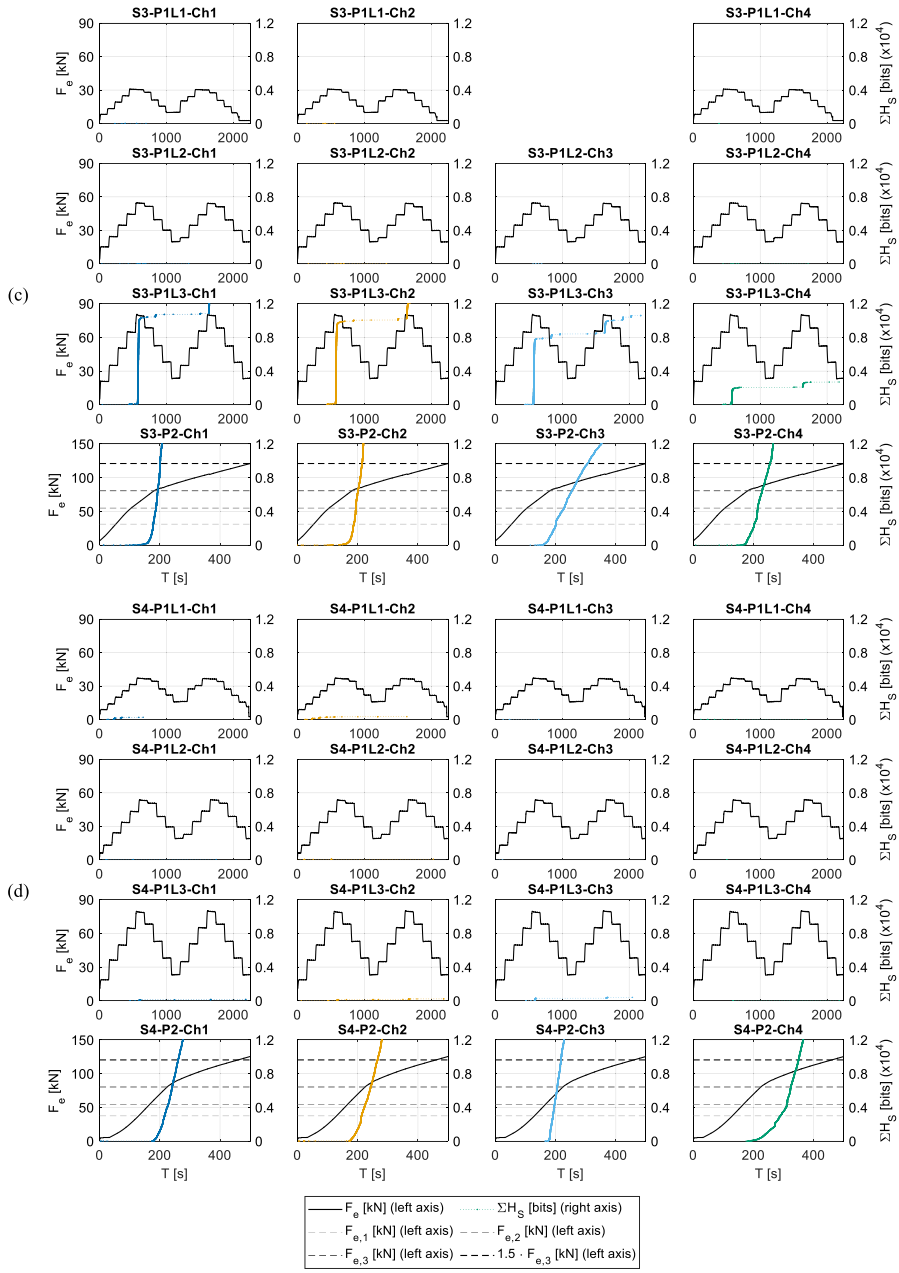


represent a positive feature for a monitoring criterion (Fig. 13).

## 4 Mechanical vs. acoustic assessment and discussion

The mechanical response of the specimens is depicted in Fig. 14 in terms of $F$ vs. deflection ($\Delta$). The focus of the study is on the cracking damage, and the results yield two significant mechanical transitions: (1) microcracking initiation (low damage (LD) state achievement) and (2) macrocracking development (severe damage (SD) state achievement), associated with (1) negligible to minor effects on global response curves and (2) significant global stiffness reduction (cracked stiffness initiation). It was found that (a) S1 exhibited both LD and SD during P1L1 test, (b) S2

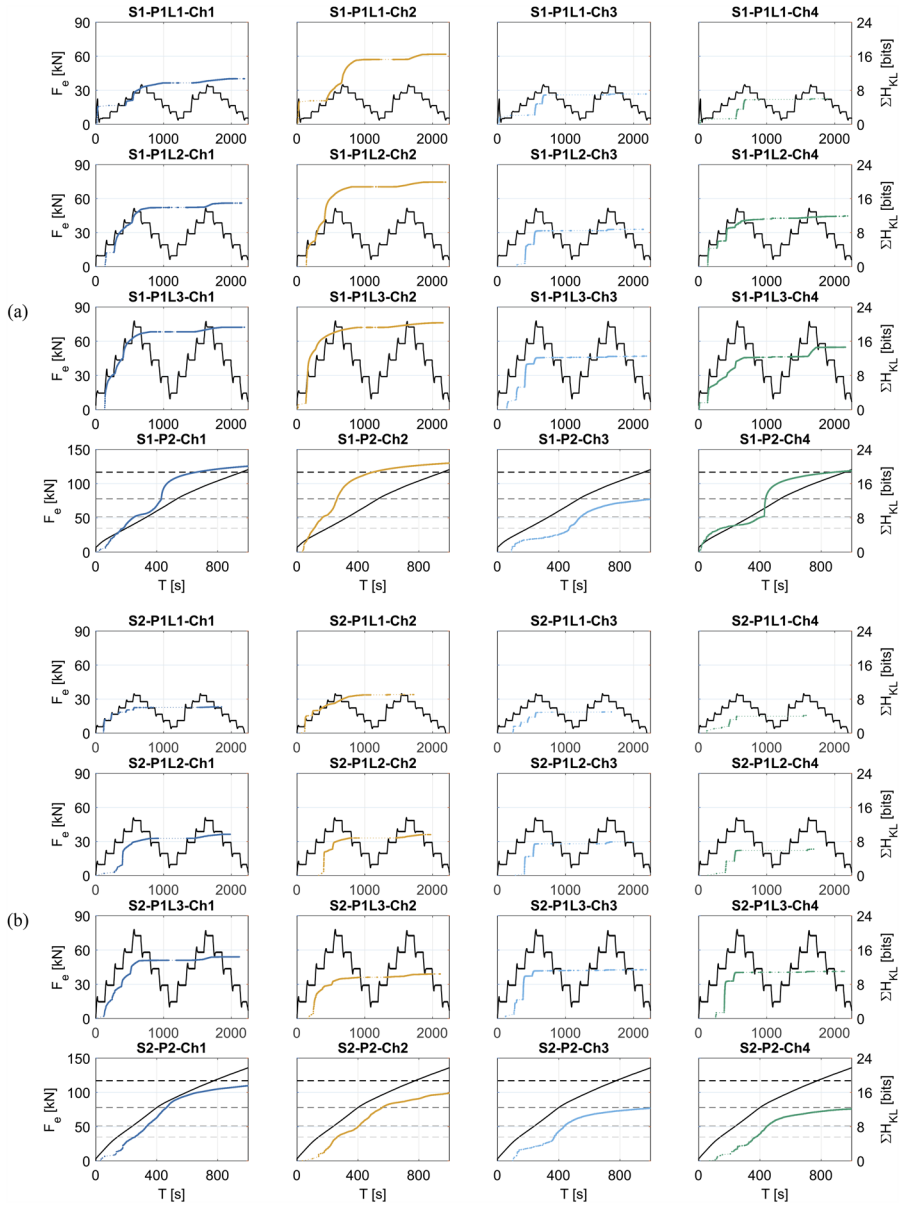


**Fig. 13** Cumulative value of Kullback–Leibler entropy ($\Sigma H_{KL}$) (MS E2.2) and recorded force ($F_e$) vs. time ($T$) for all specimens and loading protocols: **a** S1, **b** S2, **c** S3, and **d** S4

exhibited LD (SD) during P1L2 (P1L3) test, (c) S3 exhibited LD (SD) during P1L2 (P2) test, and (d) S4 exhibited LD (SD) during P1L3 (P2) test; regarding SD achievement during P2 test, for both S3 and S4, it was confirmed that this occurred prior to the exceedance of 1.5 times P1L3 maximum force level.

The acoustic activity and related features varied significantly among specimens, protocols, and channels. S1 and S2, especially S1, (S3 and S4, especially S4) were affected by significant (negligible) damage at the early loading protocols. Tests on S3 and S4 produced significant AE activity corresponding to P1L3 or P2, depending on the level of intensity. The distance from the sensor to the damaged area affects the entity of the AEs but not necessarily the qualitative characteristics and trends, suggesting that the technique is able to potentially detect damage from relatively large distances (e.g., see AEs detected by Ch3 and Ch4 over P1L1 test on specimen S1, recalling that Ch3 and Ch4 were located at about 1.8 and 2.8 m from the middle point axis).

**Fig. 13** (continued)

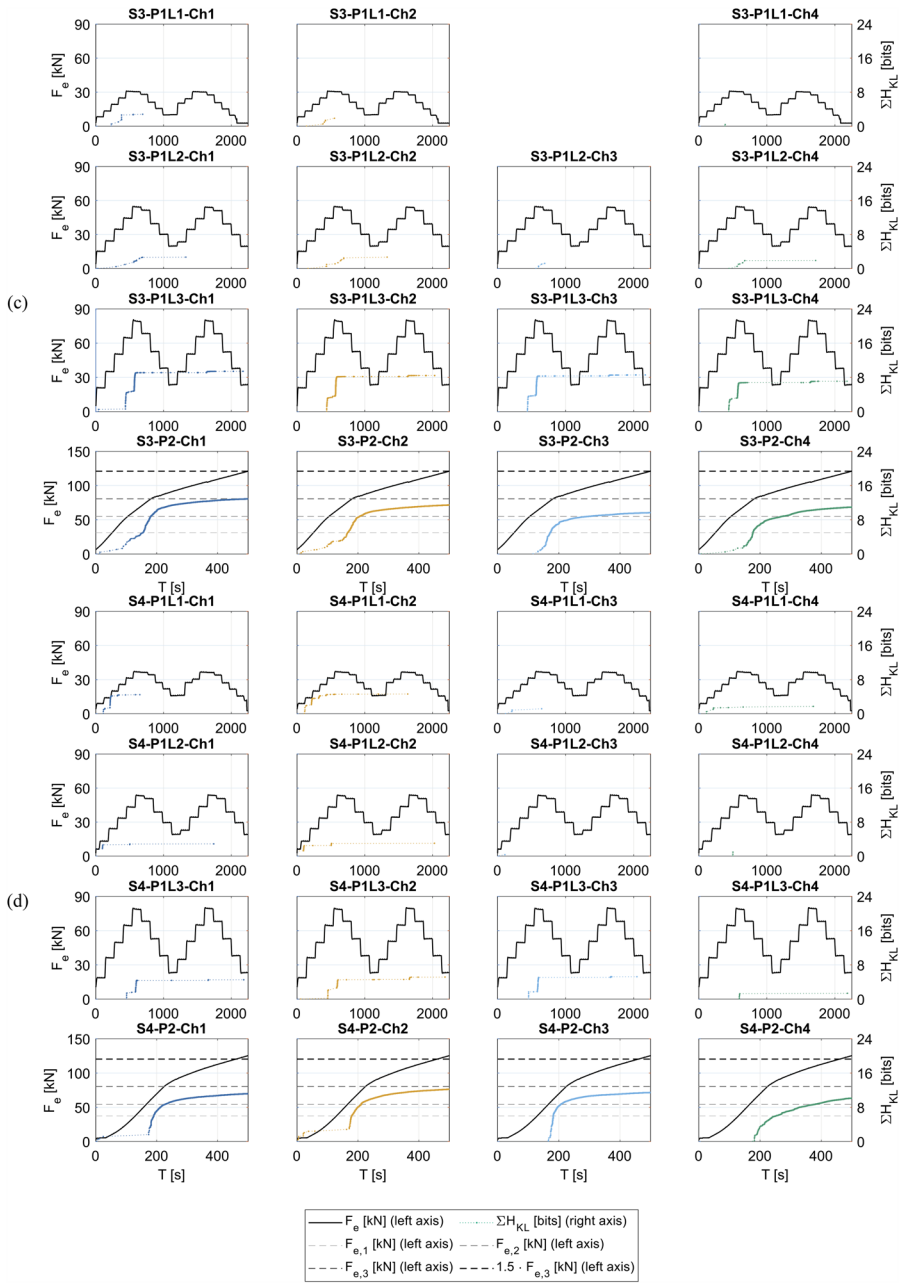


*RA* vs. *AF* (AFRA) analysis showed data migration trends that could be correlated with the damage since these qualitatively reflect the abovementioned basic AE results. In particular, simultaneous increase of *AF* and decrease of *RA* were found to be consistent with the abovementioned AE activity trend. The experimental assessment of the damage highlights the influence of post-tensioning on the AFRA analysis, as discussed in Sect. 3.2.2. Indeed, a significant number of occurrences characterized by increasing *RA* and decreasing *AF* were found during low-intensity tests in specimens S1 and S2, which exhibited LD-SD at P1L1-P1L1 and P1L2-P1L3, respectively. However, these occurrences displayed a rather irregular trend and were not always a sufficient condition for crack initiation or propagation. Such irregularities, together with the limited correlation with damage progression, may reflect

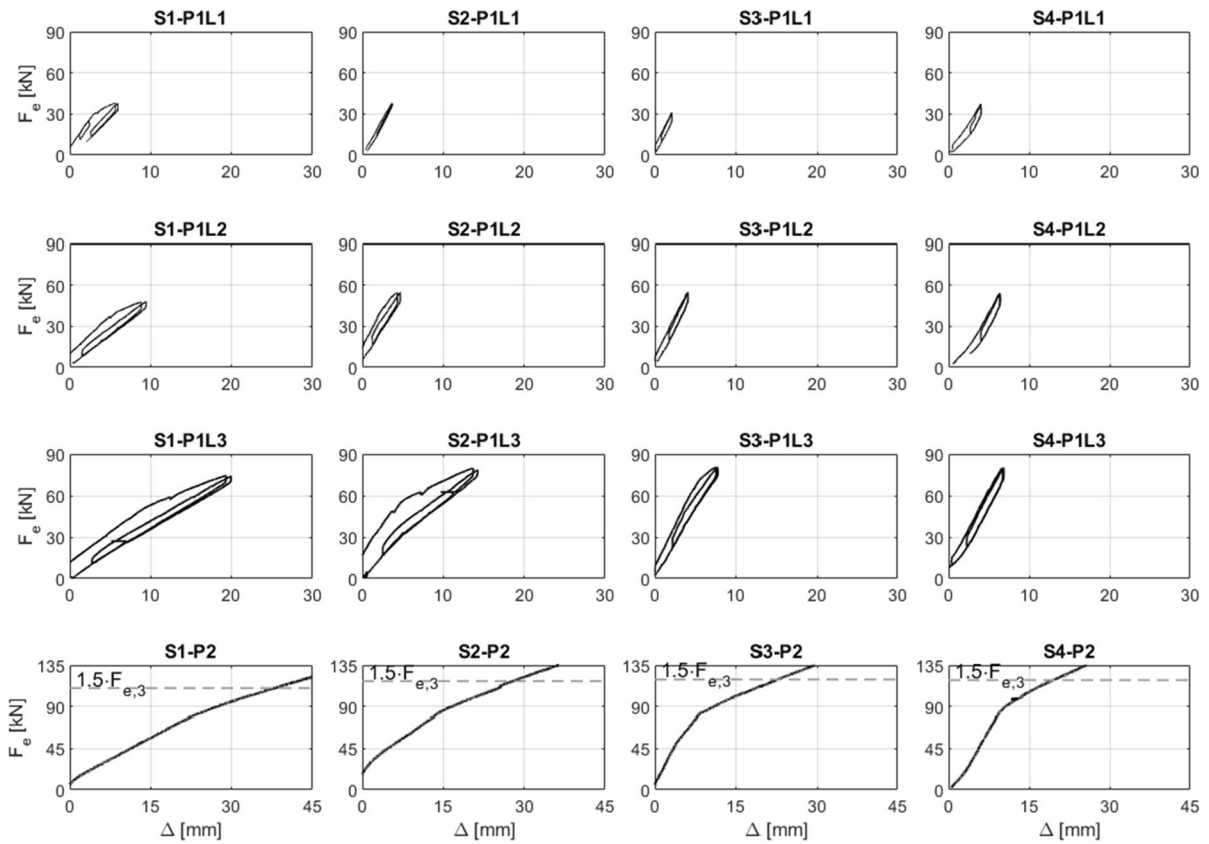


**Fig. 14** Applied force ($F_e$) vs. deflection ($\Delta$) associated with mechanical tests carried out on S1, S2, S3, and S3 specimens under P1L1, P1L2, P1L3, and P2 tests

the inherently complex stress–strain state already present under service conditions and the contribution of mechanisms not directly related to cracking, such as slip or friction. This complexity may also explain the absence of a regular increase of *AF* and decrease of *RA*, as typically observed in ordinary RC members along tensile to shear/frictional cracking evolution. Accordingly, the AFRA migration observed in the post-tensioned girders confirms the potential of this analysis as a qualitative indicator of damage evolution, while also emphasizing the need for complementary monitoring parameters to enhance its robustness. In other words, the AFRA analysis in post-tensioned girders should be interpreted, and possibly consolidated, as qualitatively reflecting the progressive severity of mixed-mode cracking and frictional or interfacial phenomena, rather than quantitatively detecting the transition from pure tensile to shear cracking.

b-value analysis showed trends to the other features even though more irregular and more difficult to interpret, likely to be potentially misunderstood. The observed lower performance can be attributed to the fact that b-value analysis mainly depends on correlations involving signal amplitude and event occurrence, parameters that are naturally more prone to noise interference and that might be more affected by the aleatory nature of AE phenomena. Other methods such as AFRA analysis or acoustic entropy might be less influenced by noisy conditions, as they inherently integrate mechanisms that act as implicit filters or data refiners. Compared to Kaiser effect/Felicity ratio and AFRA analysis, $b_{AE}$ seems to be less potentially informative regarding the damage, despite the implemented MS, especially considering the consistency among the cases. K1 (K3.2a) was found to be the most (least) sensitive to the damage condition among the investigated Kaiser effect MSs. Acoustic emission

entropy confirmed and corroborated the abovementioned trends, showing more clarity and stability of the results. $H_{KL}$ trends confirmed the expected relative nature of the formulation, accounting for relative before current state variations rather than to the absolute current entities, and $\Sigma H_{KL}$ was found to be potentially able to account for response accumulation, similarly to $H_S$ and $\Sigma H_S$.

Tests on S1 evidenced major AEs from P1L1 onwards, compatibly with experimental mechanical evidence. In particular, along the test evolution, AE testing showed Kaiser effect violation, *RA* vs. *AF* data migrations towards lower *AF* and higher *RA* values, lower b-value and v-value decreasing, and exceedance of entropy criteria. Similar results were found with regard to S2 specimens, from P1L2 onwards, also in compliance with the experimental evidence. Major AEs were observed for S3 less and more significantly under P1L2/P1L3 and P2, respectively, with trends similar to the ones associated with S1 and S2, according to the respective experimental identification of LD and SD. Finally, minor and significant acoustic activity was observed under P1L3 and P2, respectively, with exceedance of the corresponding abovementioned acoustic criteria, and this is also clearly compliant with the mechanical evidence.

## 5 Concluding remarks

The study reports methodology and results of an experimental testing campaign investigating the effectiveness of acoustic emission (AE) testing for identifying low to moderate cracking damage in reinforced concrete (RC) structures, with a focus on prestressed (post-tensioned) girders. A blind assessment of the AE data was carried out, focusing on the methodological aspects and finding (a) potential compatibility between the expected mechanical response and the observed/analyzed acoustic activity and (b) clear correlations and trends among the investigated methods and method specifications (MSs), highlighting potential strengths and weaknesses of these latter. These assessments resulted in clearly detectable tendencies, which corroborate the consistency of the experimental data and represent both the methodological backbone and the experimental dataset for performing a quantitative experimentally corroborated damage assessment procedure in future studies. Raw acoustic data are made available (Data availability section), and they represent a useful dataset that could be analyzed by other researchers.

The results demonstrate that AE testing could effectively detect and classify early and moderate cracking damage in post-tensioned prestressed RC girders, despite the complexity of their stress–strain state and behavior and also considering relatively large distances from sensors and damaged areas (e.g., larger than 1.0–1.5 m).

Kaiser effect (Felicity ratio) and Kullback entropy were found to be highly correlated with crack initiation and evolution, considering the implemented technical specification. The performance of these methods might be quantitatively explored by elaborating further the data, also accounting for uncertainty. Average frequency (*AF*) vs. rise time (RT) to amplitude (A) ratio (*RA*) (AFRA) analysis provided qualitative trends associated with damage evolution, even though in a more irregular manner; b-value analysis was the least effective and it seemed to reflect more the complexity of the mechanical configuration of the girders and the aleatory nature of AE source and propagation phenomena.

The effectiveness of AFRA and b-value analysis is expected to improve when appropriate noise-reduction techniques are applied or when the monitoring environment is relatively undisturbed, in contrast to methods that are inherently more tolerant to signal contamination, e.g., Kaiser effect and acoustic entropy. Whereas the latter methods are meant to be promising for application in SHM in situ, the former ones might be more effectively implemented as complementary tools for early damage detection within integrated structural health monitoring (SHM) systems.

The findings reflect the specimen features and the testing scenarios, as well as the number of specimens does not allow for conferring robust interpretation to the results. Future work will account for specimen and scenario uncertainty and will possibly integrate AE parameters with mechanical response data along in-situ monitoring, possibly exploring the use of the technique for SHM of bridges under service.

**Acknowledgements** The technical support of Eng. Emanuele Scaiella for the instrumental setting is fully acknowledged. *E.T.S. Sistemi Industriali Srl* (Eng. Alberto Monici) and *Vallen Systeme GmbH* are thanked for the technical and operative

support. The technical support of Eng. Dario Chiacchia for the elaborations is also acknowledged.

**Author contributions** DD: Conceptualization, Data curation, Formal analysis, Funding acquisition, Investigation, Methodology, Software, Validation, Visualization, Writing – original draft, Writing – review & editing. GM: Conceptualization, Funding acquisition, Methodology, Project administration, Resources, Supervision, Validation, Writing – review & editing.

**Funding** Open access funding provided by Università degli Studi di Napoli Federico II within the CRUI-CARE Agreement. The study was funded by the following projects: (a) Progetto di sviluppo del Dipartimento di Strutture per l'Ingegneria e l'Architettura "Dipartimento di Eccellenza" 2023–2027 (Italian Ministry of University and Research, MUR), (b) Progetto di ricerca di interesse nazionale (PRIN) 2020YKY7W4 "ENRICH: ENhancing the Resilience of Italian healthCare and Hospital facilities" (Italian Ministry of University and Research, MUR), (c) Progetto di ricerca di interesse nazionale (PRIN) 2020P5572N "FIRMITAS: multi-hazard assessment, control and retroFIt of bridges for enhanced Robustness using sMart IndusTriAlized Solutions" (Italian Ministry of University and Research, MUR), and (d) Progetto "RESIST RobustnEss aSsessment and retrofItting of bridgeS to prevenT progressive collapse under multiple hazards" (University of Naples Federico II and Compagnia di San Paolo through STAR Plus Programme 2020).

**Data availability** Raw data are freely accessible at the following link: Data repository - D'Angela and Magliulo M&S https://www.dropbox.com/scl/fo/n7ju708fmi8r4jsug9s6v/AJzokaRu9--Ql_ZorlPyr04?rlkey=x9qhky9grbkz0894kfj8zq26e&e=1&st=ugb64gne&dl=0 or by emailing the corresponding author. Further elaborated data that support the findings of this study are available from the corresponding author, [GM], upon reasonable request.

**Declarations**

**Competing interests** The authors have no financial or proprietary interests in any material discussed in this article.



## References

1. Abdel-Jaber H, Glisic B (2019) Monitoring of prestressing forces in prestressed concrete structures—an overview. Struct Control Health Monit 26:63
2. Galano S, Losanno D, Parisi F (2024) Numerical simulation of post-tensioned concrete girders with defective grouting including local stress–strain tendons response. Struct Concr 25:4515–4536. https://doi.org/10.1002/suco.202400416
3. Menga A, Kanstad T, Cantero D, Bathen L, Hornbostel K, Klausen A (2023) Corrosion-induced damages and failures of posttensioned bridges: a literature review. Struct Concr 24:84–99. https://doi.org/10.1002/suco.202200297
4. di Prisco M, Colombo M, Martinelli P (2023) Structural aspects of the collapse of a RC half-joint bridge: case of the Annone Overpass. J Bridge Eng 28:05023007. https://doi.org/10.1061/JBENF2.BEENG-6063
5. Käding M, Schacht G, Marx S (2022) Acoustic emission analysis of a comprehensive database of wire breaks in prestressed concrete girders. Eng Struct 270:114846. https://doi.org/10.1016/j.engstruct.2022.114846
6. Losanno D, Galano S, Parisi F (2024) Influence of strand rupture on flexural behavior of reduced-scale prestressed concrete bridge girders with different prestressing levels. Eng Struct 301:117358. https://doi.org/10.1016/j.engstruct.2023.117358
7. Zhang F, Yang Y, Hendriks MAN (2025) Acoustic emission-based indicators of shear failure of reinforced concrete beams without shear reinforcement. Eng Struct 330:119929. https://doi.org/10.1016/j.engstruct.2025.119929
8. D'Angela D, Ercolino M, Bellini C, Di Cocco V, Iacoviello F (2020) Characterisation of the damaging micromechanisms in a pearlitic ductile cast iron and damage assessment by acoustic emission testing. Fatigue Fract Eng Mater Struct 43:1038–1050. https://doi.org/10.1111/ffe.13214
9. Pomponi E, Vinogradov A (2013) A real-time approach to acoustic emission clustering. Mech Syst Signal Process 40:791–804. https://doi.org/10.1016/j.ymssp.2013.03.017
10. Abdelrahman M, ElBatanouny M, Dixon K, Serrato M, Ziehl P (2018) Remote monitoring and evaluation of damage at a decommissioned nuclear facility using acoustic emission. Appl Sci 8:1663. https://doi.org/10.3390/app8091663
11. Ercolino M, Farhidzadeh A, Salamone S, Magliulo G (2015) Detection of onset of failure in prestressed strands by cluster analysis of acoustic emissions. Struct Monit Mainten 2:339–355. https://doi.org/10.12989/smm.2015.2.4.339
12. Tonelli D, Luchetta M, Rossi F, Migliorino P, Zonta D (2020) Structural health monitoring based on acoustic emissions: validation on a prestressed concrete bridge tested to failure. Sensors 20:7272. https://doi.org/10.3390/s20247272
13. Ospitia N, Korda E, Kalteremidou K-A, Lefever G, Tsangouri E, Aggelis DG (2023) Recent developments in acoustic emission for better performance of structural materials.

Dev Built Environ 13:100106. https://doi.org/10.1016/j.dibe.2022.100106
14. Shiotani T, Watabe K, RILEM Technical Committee (2025) Recommendation of RILEM TC 269-IAM: damage assessment in consideration of repair/retrofit-recovery in concrete and masonry structures by means of innovative NDT: methods for damage assessment of concrete members utilizing active elastic wave measurements. Mater Struct. https://doi.org/10.1617/s11527-024-02525-5
15. Yuyama S, Yokoyama K, Niitani K, Ohtsu M, Uomoto T (2007) Detection and evaluation of failures in high-strength tendon of prestressed concrete bridges by acoustic emission. Constr Build Mater 21:491–500. https://doi.org/10.1016/j.conbuildmat.2006.04.010
16. Elfergani HA, Pullin R, Holford KM (2013) Damage assessment of corrosion in prestressed concrete by acoustic emission. Constr Build Mater 40:925–933. https://doi.org/10.1016/j.conbuildmat.2012.11.071
17. Anay R, Cortez TM, Jáuregui DV, ElBatanouny MK, Ziehl P (2016) On-site acoustic-emission monitoring for assessment of a prestressed concrete double-tee-beam bridge without plans. J Perform Constr Facil 30:04015062. https://doi.org/10.1061/(ASCE)CF.1943-5509.0000810
18. Jiang Z, Zhu Z, Accornero F, Lacidogna G (2025) Acoustic emission and digital image correlation evidence of size effects on the compression failure of concrete. Mag Concr Res 77:1060–1072. https://doi.org/10.1680/jmacr.25.00125
19. Vetrone J, Obregon JE, Indacochea EJ, Ozevin D (2021) The characterization of deformation stage of metals using acoustic emission combined with nonlinear ultrasonics. Measurement 178:109407. https://doi.org/10.1016/j.measurement.2021.109407
20. Zhang F, Zarate Garnica GI, Yang Y, Lantsoght E, Sliedrecht H (2020) Monitoring shear behavior of prestressed concrete bridge girders using acoustic emission and digital image correlation. Sensors 20:5622. https://doi.org/10.3390/s20195622
21. Ma G, Du Q (2020) Structural health evaluation of the prestressed concrete using advanced acoustic emission (AE) parameters. Constr Build Mater 250:118860. https://doi.org/10.1016/j.conbuildmat.2020.118860
22. Elbatanouny E, Henderson A, Ai L, Ziehl P (2024) Condition assessment of prestressed concrete channel bridge girders using acoustic emission and data-driven methods. Structures 67:107008. https://doi.org/10.1016/j.istruc.2024.107008
23. Jiang Z, Zhu Z, Lacidogna G (2025) Ae monitoring of crack evolution on UHPC deck layer of a long-span cable-stayed bridge. Dev Built Environ 23:100697. https://doi.org/10.1016/j.dibe.2025.100697
24. Losanno D, Galano S, Parisi F, Pecce MR, Cosenza E (2024) Experimental investigation on nonlinear flexural behavior of post-tensioned concrete bridge girders with different grouting conditions and prestress levels. J Bridge Eng 29:04023121. https://doi.org/10.1061/JBENF2.BEENG-6466
25. European Committee for Standardization. EN 1998-1 (2004) (English): Eurocode 8: Design of structures for earthquake resistance – Part 1: General rules, seismic actions and rules for buildings n.d.
26. Ministero delle infrastrutture e dei trasporti (MIT). Aggiornamento delle “Norme tecniche per le costruzioni” (in italian) 2018
27. DYWIDAG Systems International (DSI). Post-tensioning systems, multistrand systems, bar systems, repair and strengthening. 2020
28. ACI Committee 437. 437.1R-07: Load Tests of Concrete Structures: Methods, Magnitude, Protocols, and Acceptance Criteria. Tech Doc 2007
29. Castellanos-Toro S, Panesso AM, Marulanda J, Ortiz AR, Cruz A, Thomson P (2023) Evaluation of experimental techniques for performance estimation of post-tensioned concrete beams. Constr Build Mater 393:132131. https://doi.org/10.1016/j.conbuildmat.2023.132131
30. ElBatanouny MK, Ziehl PH, Larosche A, Mangual J, Matta F, Nanni A (2014) Acoustic emission monitoring for assessment of prestressed concrete beams. Constr Build Mater 58:46–53. https://doi.org/10.1016/j.conbuildmat.2014.01.100
31. Worley R, Dewoolkar MM, Xia T, Farrell R, Orfeo D, Burns D et al (2019) Acoustic emission sensing for crack monitoring in prefabricated and prestressed reinforced concrete bridge girders. J Bridge Eng 24:04019018. https://doi.org/10.1061/(ASCE)BE.1943-5592.0001377
32. RILEM Technical Committee (2010) Recommendation of RILEM TC 212-ACD: acoustic emission and related NDE techniques for crack detection and damage evaluation in concrete*: measurement method for acoustic emission signals in concrete. Mater Struct 43:1177–1181. https://doi.org/10.1617/s11527-010-9638-0
33. Grosse CU, Ohtsu M, Aggelis DG, Shiotani T (2022) Acoustic emission testing: basics for research–applications in engineering. Springer, Cham
34. Kaiser J (1950) Untersuchungen über das Auftreten von Geräuschen beim Zugversuch
35. Fowler TJ (1977) Acoustic emission testing of fiber reinforced plastics. In: Proceedings of ASCE Fall Conv. Exhib., vol. Preprint 3092, San Francisco, CA, pp 1–16
36. Kocur GK, Vogel T (2010) Classification of the damage condition of preloaded reinforced concrete slabs using parameter-based acoustic emission analysis. Constr Build Mater 24:2332–2338. https://doi.org/10.1016/j.conbuildmat.2010.05.003
37. Tsangouri E, Remy O, Boulpaep F, Verbruggen S, Livitsanos G, Aggelis DG (2019) Structural health assessment of prefabricated concrete elements using acoustic emission: towards an optimized damage sensing tool. Constr Build Mater 206:261–269. https://doi.org/10.1016/j.conbuildmat.2019.02.035
38. Zhiwei L, Paul HZ (2009) Evaluation of reinforced concrete beam specimens with acoustic emission and cyclic load test methods. Struct J 5:106
39. Ono K, Gallego A (2012) Research and applications of AE on advanced composites. J Acoust Emiss 6:180–229
40. Shetty N, Livitsanos G, Van Roy N, Aggelis DG, Van Hemelrijck D, Wevers M et al (2019) Quantification of progressive structural integrity loss in masonry with acoustic emission-based damage classification. Constr

Build Mater 194:192–204. https://doi.org/10.1016/j.conbuildmat.2018.10.215
41. Chen Y, Wei Z, Zhang Q (2012) Experimental study on Felicity effect of acoustic emission in rock under cyclic loading and tiered cyclic loading. J China Coal Soc 6:226–30
42. Behnia A, Chai HK, Shiotani T (2014) Advanced structural health monitoring of concrete structures with the aid of acoustic emission. Constr Build Mater 65:282–302. https://doi.org/10.1016/j.conbuildmat.2014.04.103
43. Fowler TJ, Blessing JA, Conlisk PJ (1989) New directions in testing. In: Proc AECM-3 Int Symp Acoust Emiss Compos Mater, Paris, France, pp 16–27
44. ASTM International (2022) Standard Practice for Determining Damage-Based Design Stress for Glass Fiber Reinforced Plastic (GFRP) Materials Using Acoustic Emission. vol. https://doi.org/10.1520/E2478-11R22
45. RILEM Technical Committee (Masayasu Ohtsu)**. Recommendation of RILEM TC 212-ACD: acoustic emission and related NDE techniques for crack detection and damage evaluation in concrete*: Test method for damage qualification of reinforced concrete beams by acoustic emission. Mater Struct 2010;43:1183–6. https://doi.org/10.1617/s11527-010-9639-z
46. ASTM International (2017) ASTM E1316-17a, Standard Terminology for Nondestructive Examinations
47. Wulan T, Li G, Huo Y, Zhao F, Yu J, Chang J et al (2024) Study on the meso-damage characteristics of RC beam under shear failure based on acoustic emission and numerical analysis. J Build Eng 96:110341. https://doi.org/10.1016/j.jobe.2024.110341
48. Lovejoy SC (2006) Development of acoustic emissions testing procedures applicable to conventionally reinforced concrete deck girder bridges subjected to diagonal tension crackin. Doctoral thesis. Oregon State University
49. Aggelis DG (2011) Classification of cracking mode in concrete by acoustic emission parameters. Mech Res Commun 38:153–157. https://doi.org/10.1016/j.mechrescom.2011.03.007
50. Ohno K, Ohtsu M (2010) Crack classification in concrete based on acoustic emission. Constr Build Mater 24:2339–2346. https://doi.org/10.1016/j.conbuildmat.2010.05.004
51. Prem PR, Murthy AR (2017) Acoustic emission monitoring of reinforced concrete beams subjected to four-point-bending. Appl Acoust 117:28–38. https://doi.org/10.1016/j.apacoust.2016.08.006
52. Zhang D, Zhang S, Chayan SM, Fan Y, Shah SP, Zheng J (2025) Acoustic emission characteristics of concrete beam with different reinforcements during bending and damage process. Mater Struct. https://doi.org/10.1617/s11527-025-02690-1
53. Zhang F, Yang Y, Fennis SAAM, Hendriks MAN (2022) Developing a new acoustic emission source classification criterion for concrete structures based on signal parameters. Constr Build Mater 318:126163. https://doi.org/10.1016/j.conbuildmat.2021.126163
54. Aggelis DG (2013) Wave propagation through engineering materials; assessment and monitoring of structures through non-destructive techniques. Mater Struct 46:519–532. https://doi.org/10.1617/s11527-013-0020-x
55. Gutenberg B, Richter CF (1944) Frequency of earthquakes in California. Bull Seism Soc Am 34:185–188
56. Colombo IS, Main IG, Forde MC (2003) Assessing damage of reinforced concrete beam using " $b$ -value" analysis of acoustic emission signals. J Mater Civ Eng 15:280–6
57. Shiotani T, Fujii K, Aoki T, Amou K (1994) Evaluation of progressive failure using AE sources and improved b-value on slope model tests. Prog Acoust Emiss 6:529–34
58. Carpinteri A, Lacidogna G, Puzzi S (2009) From criticality to final collapse: evolution of the "b-value" from 1.5 to 1.0. Chaos Solitons Fractals 41:843–853. https://doi.org/10.1016/j.chaos.2008.04.010
59. Aggelis DG, Shiotani T (2022) Parameters Based AE Analysis. In: Grosse CU, Ohtsu M, Aggelis DG, Shiotani T (eds) Acoust Emiss Test. Springer, Cham, pp 45–71
60. Iturrioz I, Lacidogna G, Carpinteri A (2014) Acoustic emission detection in concrete specimens: experimental analysis and lattice model simulations. Int J Damage Mech 23:327–358. https://doi.org/10.1177/1056789513494232
61. Rao MVMS, Prasanna Lakshmi KJ (2005) Analysis of b-value and improved b-value of acoustic emissions accompanying rock fracture. Curr Sci 89:1577–1582
62. Kahirdeh A, Khonsari M (2016) Acoustic entropy of the materials in the course of degradation. Entropy 18:280. https://doi.org/10.3390/e18080280
63. Shannon CE (1948) A mathematical theory of communication. Bell Syst Tech J 27:379–423. https://doi.org/10.1002/j.1538-7305.1948.tb01338.x
64. Burud NB, Chandra Kishen JM (2021) Non-extensive statistical mechanics for acoustic emission in disordered media: entropy, size effect, and self-organization. Int J Mech Sci 202:106514. https://doi.org/10.1016/j.ijmecsci.2021.106514
65. D'Angela D, Ercolino M, Bellini C, Di Cocco V, Iacoviello F (2021) Failure criteria for real-time assessment of ductile cast irons subjected to various loading conditions. Smart Mater Struct 30:017001. https://doi.org/10.1088/1361-665X/abc56f
66. Karimian SF, Modarres M, Bruck HA (2020) A new method for detecting fatigue crack initiation in aluminum alloy using acoustic emission waveform information entropy. Eng Fract Mech 223:106771. https://doi.org/10.1016/j.engfracmech.2019.106771
67. Nguyen T-K, Ahmad Z, Kim J (2022) Comparison of health indicators construction for concrete structure using acoustic emission hit and Kullback-Leibler divergence. In: Dang TK, Küng J, Chung TM (eds) Future Data Secur. Eng. Big Data Secur. Priv. Smart City Ind. 40 Appl., vol. 1688, Singapore: Springer, pp 603–13. https://doi.org/10.1007/978-981-19-8069-5_41.
68. Chang X, Wu S, Wang J, Fu X (2024) Investigating the comprehensive index of acoustic emissions and fractal characteristics of damage of red sandstone based on information entropy. J Nondestruct Eval 43:36. https://doi.org/10.1007/s10921-024-01051-2
69. Dangela D, Ercolino M (2021) Acoustic emission entropy: An innovative approach for structural health monitoring of fracture-critical metallic components subjected to fatigue loading. Fatigue Fract Eng Mater Struct 5(5):ffe3412

70. Kullback S, Leibler RA (1951) On information and sufficiency. Ann Math Stat 22:79–86. https://doi.org/10.1214/aoms/1177729694
71. Kahirdeh A, Sauerbrunn C, Yun H, Modarres M (2017) A parametric approach to acoustic entropy estimation for assessment of fatigue damage. Int J Fatigue 100:229–237. https://doi.org/10.1016/j.ijfatigue.2017.03.019
72. Hu Q, Chen G, Sun X, Li Y, Liu G (2024) Effect of grouting on damage and fracture characteristics of fractured rocks under mode I loading. Constr Build Mater 418:135376. https://doi.org/10.1016/j.conbuildmat.2024.135376
73. Rather AI, Laskar A, Banerjee S (2025) Monitoring bond degradation and predicting failure modes in GFRP-reinforced concrete beams using information entropy analysis of acoustic emission waveforms. Constr Build Mater 498:144014. https://doi.org/10.1016/j.conbuildmat.2025.144014
74. Hosseini SM, Azadi M, Ghasemi-Ghalebahman A, Jafari SM (2023) Fatigue crack initiation detection in ductile cast iron crankshaft under rotating bending fatigue test using the acoustic emission entropy method. Eng Fail Anal 144:106981. https://doi.org/10.1016/j.engfailanal.2022.106981
75. Christensen CO, Zhang F, Garnica GZ, Lantsoght EOL, Goltermann P, Schmidt JW (2022) Identification of stop criteria for large-scale laboratory slab tests using digital image correlation and acoustic emission. Infrastructures 7:36. https://doi.org/10.3390/infrastructures7030036
76. Zarate Garnica GI, Lantsoght EOL, Yang Y, Hendriks MAN (2024) Shear stop criteria for reinforced concrete slab strips. Bridge Maint Saf Manag Digit Sustain. 1st ed., London: CRC Press; pp 341–9. https://doi.org/10.1201/9781003483755-36.
77. Porter K, Kennedy R, Bachman R (2007) Creating fragility functions for performance-based earthquake engineering. Earthq Spectra 23:471–489. https://doi.org/10.1193/1.2720892